

PatchGuard: Provable Defense against Adversarial Patches Using Masks on Small Receptive Fields

Chong Xiang, Arjun Nitin Bhagoji, Vikash Sehwal, Prateek Mittal
Princeton University
{cxiang, abhagoji, vvikash, pmittal}@princeton.edu

Abstract—Localized adversarial patches aim to induce misclassification in machine learning models by arbitrarily modifying pixels within a restricted region of an image. Such attacks can be realized in the physical world by attaching the adversarial patch to the object to be misclassified. In this paper, we propose a general defense framework called PatchGuard that can achieve both high clean accuracy and provable robustness against localized adversarial patches. The cornerstone of PatchGuard is to use convolutional networks with small receptive fields that impose a bound on the number of features corrupted by an adversarial patch. Given a bound on the number of corrupted features, the problem of designing an adversarial patch defense reduces to that of designing a secure feature aggregation mechanism. Towards this end, we present our *robust masking* defense that robustly detects and masks corrupted features to recover the correct prediction. Our defense achieves state-of-the-art *provable* robust accuracy on ImageNette (a 10-class subset of ImageNet), ImageNet, and CIFAR-10 datasets. Against the strongest untargeted white-box adaptive attacker, we achieve 92.4% clean accuracy and 85.2% provable robust accuracy on 10-class ImageNette images against an adversarial patch consisting of 2% image pixels, 51.9% clean accuracy and 14.4% provable robust accuracy on 1000-class ImageNet images against a 2% pixel patch, and 80.0% clean accuracy and 62.2% provable accuracy on CIFAR-10 images against a 2.4% pixel patch.¹

I. INTRODUCTION

Machine learning models are vulnerable to evasion attacks, where an adversary introduces a small perturbation to a test example for inducing model misclassification [1], [2]. Many prior attacks and defenses focus on the classic setting of adversarial examples that have a small L_p distance to a benign example [1]–[12]. However, in the physical world, the classical L_p setting may require global perturbations to an object, which is not always practical. In this paper, we focus on the threat of *localized adversarial patches*, in which the adversary can arbitrarily modify pixels within a small restricted area such that the perturbation can be realized by attaching an adversarial patch to the victim object. Brown et al. [13] generate physical adversarial patches that can hijack the model prediction to a targeted class. Karmon et al. [14] propose the LaVAN attack that crafts adversarial patches in the digital domain. Eykholt et al. [15] demonstrate a robust physical world attack that attaches small stickers to a stop sign for fooling traffic sign classification.

The success of practical localized adversarial patches has inspired several defense approaches. Digital Watermark

(DW) [16] aims to detect and remove the adversarial patch while Local Gradient Smoothing (LGS) [17] proposes smoothing the suspicious region of pixels to neutralize the adversarial patch. However, these empirical defenses are heuristic approaches and lack robustness against a strong adaptive attacker [18], leading to the development of several certified defenses. Chiang et al. [18] propose the first certified defense against adversarial patches via Interval Bound Propagation (IBP) [19], [20]. Zhang et al. [21] use a clipped BagNet to achieve provable robustness, and Levine et al. [22] propose De-randomized Smoothing (DS) to further improve provable robustness. While these works are in the same spirit as ours, prior certified defenses struggle with poor clean accuracy and provable robustness.

In this paper, we propose a general defense framework called PatchGuard that achieves *substantial provable robustness while maintaining high clean accuracy against localized adversarial patches*. The cornerstone of our defense framework involves the use of a convolutional neural network (CNN) with a small receptive field that imposes a bound on the number of features that can be corrupted due to an adversarial patch. The receptive field of a CNN is the region of an input image that a particular feature is influenced by, and model prediction is based on the aggregation of features extracted from different regions of an image. An example of the receptive field is shown as the red box on the image in Figure 1. Our case study in Section III-A demonstrates that a large receptive field makes CNNs more vulnerable to adversarial patch attacks. For a model with a large receptive field of 483×483 (ResNet-50 [23]) on ImageNet images [24], a small patch with 3% corrupted image pixels is present in the receptive field of most extracted features and can thus easily change model prediction. A small receptive field, on the other hand, limits the number of corrupted features, and we use it as the fundamental building block of robust classifiers. We note that a small receptive field is not a barrier to achieving high clean accuracy. A ResNet-like architecture with a small 17×17 receptive field can achieve an AlexNet-level accuracy for ImageNet top-5 classification [25]. The potential robustness improvement, as well as the moderate accuracy drop, motivates the use of small receptive fields in our defense framework.

However, a small receptive field alone is not enough for robust prediction since conventional models use insecure feature aggregation mechanisms such as mean or sum. The use of small receptive fields turns the problem of designing an

¹Our code is available at <https://github.com/inspire-group/PatchGuard> for the purpose of reproducibility.

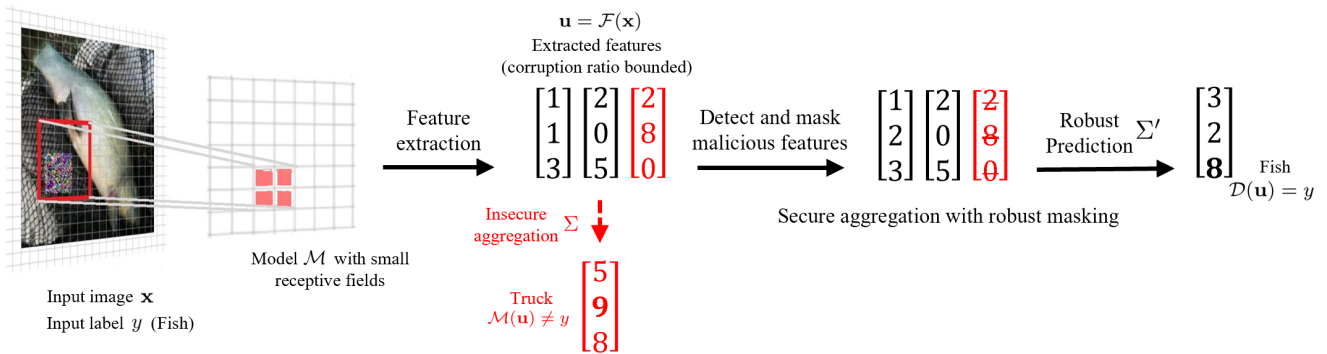


Fig. 1. **Overview of defense.** The small receptive field bounds the number of corrupted features (one out of three vectors in this example). The one corrupted feature (red vector) in this example has an abnormally large element that dominates the insecure aggregation (Σ) but also leads to a distinct pattern from clean features. Our *robust masking* aggregation detects and masks the corrupted feature, recovering the correct prediction from the remaining features.

adversarial patch defense into a secure aggregation problem, and we propose *robust masking* as an instance of the secure feature aggregation mechanism. Figure 1 provides an overview of our defense. The small receptive field ensures that only a small fraction of extracted features are corrupted due to an adversarial patch. A small number of corrupted features require the adversary to create abnormally large feature values to dominate the final prediction, and *robust masking* aims to detect and mask the abnormal features. Our empirical analysis shows that removing a small number of features of a clean image rarely changes model prediction. Therefore, we are likely to recover the correct prediction if all the corrupted features are masked. Robust masking thus introduces a fundamental dilemma for the adversary: either be detected by our defense or fail to generate an effective adversarial patch. In Section IV, we show that this dilemma leads to a proof of *provable robustness* for our defense, providing the guarantee that the model can always recover correct predictions on certified images for any adversarial patch. This is a stronger notion of robustness compared with defenses that only detect the adversarial attack [7], [8], [26]. We note that PatchGuard subsumes several existing defenses [21], [22] (as shown in Section VI-A), and has the best performance due to the use of *robust masking*.

We consider the strongest threat model of adversarial patch attacks, where the adversarial patch can be placed on any part of the image, including on top of salient objects, and evaluate our defense against the strongest white-box untargeted adaptive attacker on ImageNette (a 10-class subset of ImageNet) [27], 1000-class ImageNet [24], and CIFAR-10 [28] datasets. We achieve 92.4% clean accuracy and 85.2% provable robust accuracy on 10-class ImageNette images against an adversarial patch consisting of 2% image pixels, 51.9% clean accuracy and 14.4% provable robust accuracy on 1000-class ImageNet images against a 2% pixel patch, and 80.0% clean accuracy and 62.2% provable accuracy on CIFAR-10 images against a 2.4% pixel patch. Our defense achieves state-of-the-art provable robustness on all three datasets compared to previous defenses [18], [21], [22]. Our main contributions

can be summarized as follows:

- 1) We demonstrate the use of a small receptive field as a fundamental robustness building block and integrate it into a general defense framework called PatchGuard. PatchGuard is flexible and general as it is compatible with any network with small receptive fields and any secure aggregation mechanism.
- 2) We present *robust masking* as an instance of the secure aggregation mechanism that has provable robustness and recovers correct predictions for certified images against any white-box adaptive attacker.
- 3) We provide a comprehensive analysis of our defense across 3 realistic image datasets: ImageNette, ImageNet, and CIFAR-10, and demonstrate state-of-the-art provable robust accuracy.

II. PROBLEM FORMULATION

In this section, we lay out the notation and terminology used in this paper and formulate the localized adversarial patch attack, including the attacker’s objective, capability, knowledge, and the algorithm used for adversarial patch generation.

A. Notation and Terminology

We focus on fully convolutional neural networks (CNNs) such as ResNet [23] and Inception [29], which use convolutional layers for feature extraction and an additional fully-connected layer for the final prediction. This structure widely is used in state-of-the-art image classification models [23], [29]–[31].

Convolutional Network. Table I provides a summary of our notation. We use $\mathcal{X} \subset [0, 1]^{W \times H \times C}$ to denote the image space where each image has width W , height H , number of channels C , and the pixel values are re-scaled to $[0, 1]$. We take $\mathcal{Y} = \{0, 1, \dots, N - 1\}$ as the class label space, where the number of classes is N . We use $\mathcal{M}(\mathbf{x}) : \mathcal{X} \rightarrow \mathcal{Y}$ to denote the model that takes an image $\mathbf{x} \in \mathcal{X}$ as input and predicts the class label $y \in \mathcal{Y}$. Let $\mathcal{F}(\mathbf{x}) : \mathcal{X} \rightarrow \mathcal{U}$ be the feature extractor that outputs the feature tensor $\mathbf{u} \in \mathcal{U} \subset \mathbb{R}^{W' \times H' \times C'}$, where W' , H' , C' are the width, height, and number of channels in this feature map, respectively. We refer to each C' -dimensional feature in

TABLE I
TABLE OF NOTATION

| Notation | Description |
|---|---|
| $\mathcal{X} \subset [0, 1]^{W \times H \times C}$ | Image space |
| $\mathcal{Y} = \{0, 1, \dots, N - 1\}$ | Label space |
| $\mathcal{U} \subset \mathbb{R}^{W' \times H' \times C'}$ | Feature space |
| $\mathcal{M}(\mathbf{x}) : \mathcal{X} \rightarrow \mathcal{Y}$ | Model predictor from $\mathbf{x} \in \mathcal{X}$ |
| $\mathcal{M}(\mathbf{u}) : \mathcal{U} \rightarrow \mathcal{Y}$ | Model predictor from $\mathbf{u} \in \mathcal{U}$ |
| $\mathcal{F}(\mathbf{x}) : \mathcal{X} \rightarrow \mathcal{U}$ | Local feature extractor for all classes |
| $\mathcal{F}(\mathbf{x}, l) : \mathcal{X} \times \mathcal{Y} \rightarrow \mathcal{U}$ | Local feature extractor for class l |
| $P \subset \{0, 1\}^{W \times H}$ | Set of binary pixel blocks in the image space |
| $W \subset \{0, 1\}^{W' \times H'}$ | Set of binary windows in the feature space |

tensor \mathbf{u} as a *local feature* since it is only extracted from part of the input image as opposed to the entire image. When the local feature tensor \mathbf{u} is the output of the last convolutional layer, conventional networks use a linear aggregation (e.g., average) over all local features to obtain the *global feature* in $\mathbb{R}^{C'}$. The global feature will then go through the last fully-connected layer (i.e., classification layer) and yield the *global logits* vector in \mathbb{R}^N , as shown in the top of Figure 2.

Local logits, confidence, and prediction tensor. In the bottom of Figure 2, we show an alternative way of computing *global logits*, which has *local logits* as the mid-product. Given the output of the last convolutional layer (in $\mathbb{R}^{W' \times H' \times C'}$), we can first feed the extracted feature tensor to the fully-connected layer to get the local logits in $\mathbb{R}^{W' \times H' \times N}$. Applying the linear aggregation to the local logits will give the same global logits tensor in \mathbb{R}^N for final prediction. We name the mid-product as *local logits* because each N -dimensional vector in the local logits tensor is based on each C' -dimensional *local feature*. Furthermore, we can derive the concept of *local confidence* and *local prediction* tensor by feeding the local logits tensor to a softmax layer and an argmax layer, respectively. In the remainder of this paper, we generalize the concept of *feature* by considering it to refer to either a logits tensor, a confidence tensor, or a prediction tensor. When this is the case, we have $C' = N$.²

Receptive field. We define the *receptive field* of a particular feature in a CNN to be a subset of image pixels that a particular local feature $\tilde{\mathbf{u}} \in \mathbb{R}^{C'}$ is looking at, or affected by. Formally, if we represent the input image x as a *set of pixels*, the receptive field of a particular local feature $\tilde{\mathbf{u}}$ is a subset of pixels for which the gradient of $\tilde{\mathbf{u}}$ is non-zero, i.e., $\{r \in x | \nabla_r \tilde{\mathbf{u}} \neq \mathbf{0}\}$. For simplicity, we use the phrase “receptive field of a CNN” to refer to “receptive field of a particular feature of a CNN”.

Notation reuse. When the feature type is one of logits, confidence, or prediction, we sometimes abuse the notation by letting $\mathcal{F}(\mathbf{x}, l) : \mathcal{X} \times \mathcal{Y} \rightarrow \mathbb{R}^{W' \times H'}$ denote the slice of the feature corresponding to class l . We call the elements of

²Some convolutional networks (e.g., AlexNet [32], VGG [31]) do not have an explicit linear aggregation layer but simply flatten the feature tensor and feed it to a fully-connected layer with large input dimensionality for model prediction. In this case, we can split the fully-connected layer into a linear aggregation layer and another fully-connected layer with smaller input dimensionality. This splitting does not change the model capacity due to the linearity of two layers.

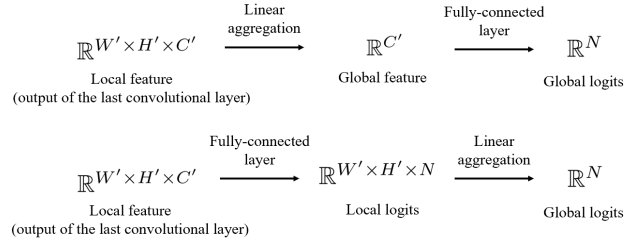


Fig. 2. Two equivalent ways of computing the global logits tensor (top: used in conventional CNNs; bottom: used in our defense).

$\mathcal{F}(\mathbf{x}, l)$ the *class evidence* for class l . We will also reuse the notation \mathcal{M} as a mapping from a hidden feature map space \mathcal{U} to the label space \mathcal{Y} . $\mathcal{M}(\mathbf{u})$ in this context implies doing model inference with a feature tensor \mathbf{u} .

B. Attack Formulation

Attack objective. We focus on evasion attacks against an image classification model. Given a deep learning model \mathcal{M} , an image \mathbf{x} , and its true class label y , the goal of the attacker is to find an image $\mathbf{x}' \in \mathcal{A}(\mathbf{x}) \subset \mathcal{X}$ satisfying a constraint \mathcal{A} such that $\mathcal{M}(\mathbf{x}') \neq y$. The constraint \mathcal{A} is defined by the attacker’s threat model, which we will describe below. This attack objective of inducing misclassification in any class apart from the true one is referred to as an *untargeted attack*. In contrast, if the attacker aims to misclassify the image to a particular target class $y' \neq y$, it is called a *targeted attack*. We use the most effective white-box LaVAN [14] attack to evaluate the accuracy of undefended models while our provable defense results *hold for any attack*.

Attacker capability. For the adversarial patch attack, the attacker can arbitrarily modify pixels within a restricted region. This restricted region can be anywhere on the image, even over the salient object, but we assume there is only one such contiguous region of a fixed size. We note that this is the strongest threat model used in the existing literature on certified defenses against adversarial patches [18], [21], [22]. Formally, we use a binary *pixel block* $\mathbf{p} \in P \subset \{0, 1\}^{W \times H}$ to represent the restricted region, where the pixels within the region are set to one. Then the constraint set $\mathcal{A}(\mathbf{x})$ can be expressed as $\{\mathbf{x}' = (\mathbf{1} - \mathbf{p}) \odot \mathbf{x} + \mathbf{p} \odot \mathbf{x}'' | \mathbf{x}, \mathbf{x}' \in \mathcal{X}, \mathbf{x}'' \in [0, 1]^{W \times H \times C}, \mathbf{p} \in P\}$, where \odot refers to the element-wise product operator, and \mathbf{x}'' is the content of the adversarial patch.

Attacker knowledge. We consider the strongest adaptive white-box attacker in this paper. The adaptive attacker has perfect knowledge of the defense mechanism, and the white-box attacker has access to model architecture and weights, as well as to the training and test data.

Attack algorithm. The adversarial patch attack can be formulated as the following optimization problem, as done in related literature [13], [14].

$$\mathbf{x}' = \arg \max_{\mathbf{x}' \in \mathcal{A}(\mathbf{x})} \mathcal{L}(\mathcal{M}(\mathbf{x}'), y) \quad (1)$$

Here we abuse the notation to let $\mathcal{M}(\mathbf{x}')$ to be the final predicted confidence vector of the model, and y to be the

one-hot encoded vector of the class. $\mathcal{L}(\cdot)$ refers to the cross-entropy loss. Since we have $\mathbf{x}' = (\mathbf{1} - \mathbf{p}) \odot \mathbf{x} + \mathbf{p} \odot \mathbf{x}''$, and \mathbf{p}, \mathbf{x} are fixed, the actual optimization is over \mathbf{x}'' , which is distinguished from conventional L_p adversary optimization [4], [5]. This optimization problem can be approximately solved with gradient-based optimization algorithms such as Stochastic Gradient Descent [33], [34].

III. PATCHGUARD

In this section, we first motivate the use of small receptive fields and secure feature aggregation (i.e., *robust masking*) in our defense. Towards this end, we analyze the behavior of the adversarial patch attack on ResNet-50 whose large receptive fields and insecure aggregation lead to high misclassification rates from small adversarial patches. Next, we will give an overview of our general defense framework called PatchGuard, followed by our use of networks with small receptive fields and details of our *robust masking* based secure aggregation.

A. Why are adversarial patches effective?

Previous work [13], [14] on adversarial patches, surprisingly, shows that model prediction can be manipulated by patches that occupy a very small portion of input images. For example, when using the LaVAN attack [14], a patch comprising of only 3% of the pixels of an image from the ImageNet dataset [24] is enough to achieve a nearly 100% untargeted attack success rate. In this subsection, we provide a case study for ResNet-50 [23] trained on ImageNet [24], ImageNette (a 10-class subset of ImageNet) [27], and CIFAR-10 [28] datasets and identify two critical reasons for the model vulnerability. These will then motivate the development and discussion of our defense.

Experiment I. Applying the feature extractor $\mathcal{F}(\cdot)$ of ResNet-50 to an input image \mathbf{x} gives us the local logits tensor in the shape of $W' \times H' \times N$, where $W' \cdot H'$ is the number of local logits in the ResNet-50 architecture, and N is the number of classes. Our first experiment aims to analyze the extent to which an adversarial patch can affect each of the $W' \cdot H'$ local logits $\tilde{\mathbf{u}} \in \mathbb{R}^N$. To do this, we modify the attack optimization objective in Equation 1 to be $\arg \max_{\mathbf{x}'} \mathcal{L}(\text{softmax}(\tilde{\mathbf{u}}), y)$, where $\tilde{\mathbf{u}}$ depends on \mathbf{x}' . We attack each $\tilde{\mathbf{u}}$ individually and record the local prediction; an incorrect local prediction indicates that the adversary can corrupt the corresponding local logits/feature. For ImageNet, we randomly select 2500 validation images for experiments. For ImageNette and CIFAR-10, we use the entire validation set. For each image, we choose a random patch location for the untargeted attack. Further details about the experiment setup are covered in Section V-A and Appendix A.

Vulnerability I: the small adversarial patch appears in the large receptive fields of most local features and is able to manipulate the local predictions. In Table II, we report the percentage of incorrect local predictions after the attack (attacked) and before the attack (original) as well as their percentage difference. We can see that a small patch in a randomly chosen location that only takes up 3% of image

TABLE II
RESULTS FOR ATTACKING LOCAL LOGITS ON THREE DATASETS

| Dataset Patch size | ImageNet 3% pixel | ImageNette 3% pixel | CIFAR-10 3% pixels |
|------------------------------------|----------------------|------------------------|-----------------------|
| Incorrect local pred. (attacked) | 84.1% | 52.8% | 68.2% |
| Incorrect local pred. (original) | 59.8% | 15.2% | 13.6% |
| Incorrect local pred. (difference) | 24.3% | 37.6% | 54.6% |
| Incorrect global predictions | 99.5% | 96.0% | 79.2% |

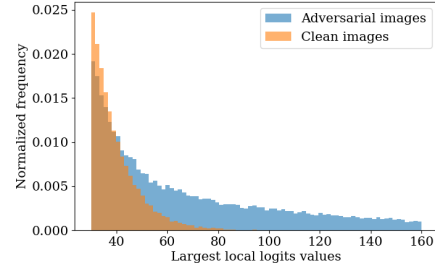


Fig. 3. Histogram of largest local logits values for adversarial and clean images for ImageNet.

pixels can corrupt 24.3% additional local predictions for ImageNet images, 37.6% for ImageNette, and 54.6% for CIFAR-10. We note that these differences will be even larger if the adversary tries all possible patch locations for optimal attack performance. Moreover, we can see that even with a single random patch location, more than 50% local predictions of the attacked images from all three datasets are incorrect, leading to incorrect global predictions when aggregated (incorrect global predictions in Table II). This vulnerability mainly stems from the large receptive field of the convolutional network. Each local feature of ResNet-50 is influenced by a 483×483 pixel region in the input space (with zero padding) [35]; therefore, even if the adversarial patch only appears in a restricted area, it is still within the receptive field of many local features and can manipulate the local predictions.³ This observation motivates the use of small receptive fields: if the receptive field is small, it ensures that only a limited number of local features can be corrupted by an adversarial patch, and robust prediction may be possible.

Experiment II. Our second experiment explores the difference in the distribution of local logits values, or class evidence, between clean and adversarial images. We use the untargeted attack introduced in Equation 1 to generate adversarial patches for the same set of images used in Experiment I. For each clean or adversarial image, we get the largest value in each of the $W' \cdot H'$ N -dimensional local logits and plot the histogram.

Vulnerability II: the small adversarial patch creates extremely large malicious local feature values and makes the

³We note that a patch appearing in the receptive field of a local feature does not necessarily indicate a successful local feature corruption. Each local feature of the convolutional network focuses exponentially more on the center of its receptive field (further details are in Appendix C) When the adversarial patch is far away from the center of the receptive field, its ability to influence the feature decreases greatly.

linear feature aggregation (e.g., average pooling) insecure.

Due to space constraints, we only plot the histogram for ImageNet in Figure 3 and include similar results for ImageNette and CIFAR-10 in Appendix B. As we can see from Figure 3, the adversarial patch tends to create extremely large malicious class evidence to increase the chance of a successful attack. Conventional convolutional networks use simple linear operations such as average pooling to aggregate all local features, and thus are vulnerable to these large malicious feature values. This observation motivates our development of *robust masking* as a secure feature aggregation mechanism.

B. Overview of PatchGuard

In Section III-A, we identified the large receptive field and insecure aggregation of convolutional networks as two major sources of model vulnerability. In this subsection, we provide an overview of our defense that tackles both problems. Our goal is to propose a defended model \mathcal{D} such that $\mathcal{D}(\mathbf{x}) = \mathcal{D}(\mathbf{x}') = y$ for any clean data point $(\mathbf{x}, y) \in \mathcal{X} \times \mathcal{Y}$ and adversarial example $\mathbf{x}' \in \mathcal{A}(\mathbf{x})$, where $\mathcal{A}(\mathbf{x})$ is the adversarial constraint introduced in Section II-B. Note that the goal of our defense is to *recover the correct prediction*, which is harder than merely detecting an attack.

Figure 1 provides an overview of our defense framework. We consider a convolutional network \mathcal{M} with small receptive fields. The feature extractor $\mathcal{F}(\mathbf{x})$ produces the local feature tensor \mathbf{u} extracted from each small region of the input image \mathbf{x} , where \mathbf{u} can be any one of logits, confidence or the model prediction tensor in our defense. Our defense framework is compatible with any convolutional network with small receptive fields, and we will present two general ways of building such networks in Section III-C. The small receptive field ensures that only a small fraction of features are corrupted by a localized adversarial patch. However, the insecure aggregation of these features via average pooling or summation might still result in misclassification $\mathcal{M}(\mathbf{u}) \neq y$. To address this vulnerability, we propose a *robust masking* algorithm for secure feature aggregation.

In *robust masking*, we detect and mask the corrupted features in the local feature tensor $\mathbf{u} = \mathcal{F}(\mathbf{x})$. Since the number of corrupted local features is limited due to the small receptive field, the adversary is forced to create large feature values to dominate the global prediction. These large feature values lead to a distinct pattern and enable our detection of corrupted features. Further, our empirical analysis in Section V-C shows that model predictions on clean images are invariant to the removal of partial features. Therefore, once the corrupted features are masked, we are likely to recover the correct prediction y with $\mathcal{D}(\mathbf{u})$ computed using the remaining local features, as shown in the right part of Figure 1. This defense introduces a dilemma for the adversary: either be detected by our defense or fail to generate an effective adversarial patch. Such a dilemma enables *provable robustness*. We will introduce the defense details in Section III-D, and perform its provable security analysis in Section IV.

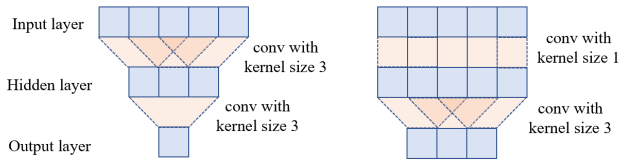


Fig. 4. Effect of the convolution kernel size on the output receptive field size (left: two convolutions with a kernel size of 3; right: two convolutions with a kernel size of 1 and 3, respectively).

C. Convolutional Networks with Small Receptive Fields

As mentioned in Section III-B, our defense framework is *compatible with any network with small receptive fields*. In this subsection, we discuss two general ways to build a model with small receptive fields. Our goal is to reduce the number of image pixels that can affect a particular feature.

Building an ensemble model. The most straightforward way to design a network with small receptive fields is to divide the original image into multiple small pixel patches and feed each pixel patch to a *base* model for separate classification. We can then build an *ensemble* model whose output is the aggregation of the output of *base* models. In this ensemble model, a local feature is the base model output, which can be logits, confidence, or prediction. Since the base model only takes a small pixel patch as input, each local feature is only affected by a small number of pixels, and thus the ensemble model has a small receptive field. We note that the number of all possible small pixel patches is a quadratic function of the image size. As the image resolution becomes higher, the training and testing computation cost of the ensemble model increases greatly. A natural approach to reduce computation cost is to do inference on a sub-sampled set of small pixel patches.

Using small convolution kernels. An elegant solution to the challenge of computation cost in the above approach is to use small convolution kernels in conventional CNN architectures. In Figure 4, we provide a toy example for 1-D convolution computation with different kernel sizes. As we can see, the output cell is affected by all 5 input cells when using two convolutions with a kernel size of 3 (left) while each output cell is only affected by 3 input cells when reducing the size of one kernel to 1 (right). This logic extends directly to the large CNNs used in practice by replacing large convolution kernels with small kernels. Moreover, we can use a large convolution stride to skip a portion of small pixel patches to reduce the computation cost. The modified CNN can be regarded as an ensemble model from a subset of all possible pixel patches. With this formulation, we can efficiently extract all local features with one-time model feed-forward computation. We will instantiate both approaches using the implementation from Levine et al. [36] and Brendel et al. [37] in our evaluation and compare their performance in terms of accuracy and efficiency.

Algorithm 1 Robust masking

Input: Image \mathbf{x} , model \mathcal{M} , feature extractor \mathcal{F} , clipping bound $[c_l, c_h]$, the set of sliding windows \mathcal{W} , and detection threshold T .

Output: Robust prediction y

```

1: procedure ROBUSTMASKING
2:    $\bar{y} \leftarrow \mathcal{M}(\mathbf{x})$   $\triangleright$  Model prediction  $\bar{y}$ 
3:    $\mathbf{u}_{\bar{y}} \leftarrow \mathcal{F}(\mathbf{x}, \bar{y})$   $\triangleright$  Local feature tensor for class  $\bar{y}$ 
4:    $\hat{\mathbf{u}}_{\bar{y}} \leftarrow \text{CLIP}(\mathbf{u}_{\bar{y}}, c_l, c_h)$   $\triangleright$  Clipped local features  $\hat{\mathbf{u}}_{\bar{y}}$ 
5:    $\mathbf{w}^* \leftarrow \text{DETECT}(\hat{\mathbf{u}}_{\bar{y}}, T, \mathcal{W})$   $\triangleright$  Suspicious window  $\mathbf{w}^*$ 
6:   if  $\mathbf{w}^* \neq \perp$  then
7:      $y \leftarrow \mathcal{M}(\mathcal{F}(\mathbf{x}) \odot (\mathbf{1} - \mathbf{w}^*))$   $\triangleright$  Masked prediction
8:   else
9:      $y \leftarrow \bar{y}$   $\triangleright$  Retained original prediction
10:  end if
11:  return  $y$ 
12: end procedure

13: procedure DETECT( $\hat{\mathbf{u}}_{\bar{y}}, T, \mathcal{W}$ )
14:   $\mathbf{w}^* \leftarrow \arg \max_{\mathbf{w} \in \mathcal{W}} \text{SUM}(\mathbf{w} \odot \hat{\mathbf{u}}_{\bar{y}})$   $\triangleright$  Detection
15:   $t \leftarrow \text{SUM}(\mathbf{w}^* \odot \hat{\mathbf{u}}_{\bar{y}}) / \text{SUM}(\hat{\mathbf{u}}_{\bar{y}})$   $\triangleright$  Normalization
16:  if  $t \leq T$  then
17:     $\mathbf{w}^* \leftarrow \perp$   $\triangleright$  Return  $\perp$  if not exceeding threshold  $T$ 
18:  end if
19:  return  $\mathbf{w}^*$ 
20: end procedure

```

D. Robust Masking

Given that an adversarial patch can only corrupt a limited number of local features with small receptive fields, the adversary is forced to create a small region of abnormally high feature values to induce misclassification. We aim to detect and mask this corrupted region so that the final classification is not influenced by these adversarial feature values. We will then recover the correct prediction as long as clean images are prediction invariant to feature masking, which we demonstrate is indeed the case for the state-of-the-art models we consider. Moreover, the prediction invariance can also improve the clean accuracy of our defense when a benign region is falsely detected. The defense algorithm is shown in Algorithm 1. It takes a clean or adversarial image as its input and aims to output the correct prediction.

Clipping. As shown in Algorithm 1, the first step of our defense is to get the class prediction \bar{y} and its corresponding clipped local feature tensor $\hat{\mathbf{u}}_{\bar{y}}$ from the undefended model. The values of the clipping bounds c_l, c_h depend on the type of feature we are using. If we use logits, we will set $c_l = 0, c_h = \infty$ by default. We clip the negative values to zero since our empirical analysis in Section V-C shows that they make little contribution to the correct prediction of clean images but can be abused by the adversary to reduce the class evidence of the true class. If the feature refers to confidence tensor or one-hot encoded prediction, the clipping is optional, or equivalently $c_l = 0, c_h = 1$, since the range of the feature

values is already bounded.

Detection. We use the subprocedure DETECT to examine the clipped local feature tensor $\hat{\mathbf{u}}_{\bar{y}}$ and detect the malicious region. DETECT takes the feature tensor $\hat{\mathbf{u}}_{\bar{y}}$, the normalized detection threshold $T \in [0, 1]$, and a set of sliding windows \mathcal{W} as inputs. A window is a binary mask in the feature space whose size is determined by the number of local features that can be corrupted by the adversarial patch. Formally, let p be the patch size, r be the size of receptive field, and s be the stride of receptive field, which is the pixel distance between two adjacent receptive centers, we can compute the window size w as

$$w = \lceil (p + r - 1) / s \rceil \quad (2)$$

This equation can be derived by considering the largest patch that will appear in w but not $w+1$ receptive fields. More details of this equation are covered in Appendix C. We represent each window \mathbf{w} with a binary feature map in $\{0, 1\}^{W' \times H'}$, where features within the window have values of one. This representation is essentially the same as the binary *pixel block* mentioned in Section II-B, except that window is for local feature tensor but *pixel block* is for input image tensor. We use different terms to avoid potential confusion. To detect the malicious region, DETECT calculates the sum of feature values, or class evidence for class \bar{y} , within every possible window and identifies the window with the highest sum of class evidence. If the normalized highest class evidence exceeds the threshold T , we return the corresponding window \mathbf{w}^* as the suspicious window; otherwise, we return \perp .

Masking. If we detect a suspicious area in the local feature space, we remove the suspicious features and do prediction on the masked features to get $y = \mathcal{M}(\mathcal{F}(\mathbf{x}) \odot (\mathbf{1} - \mathbf{w}^*))$. Our empirical analysis shows that clean image predictions are usually invariant to such feature masking; therefore, this masking operation provides us with a robust classification model rather than a simple detection defense. Moreover, our defense is able to retain high clean accuracy, because even if we incorrectly detect and remove suspicious features of a clean image, the model is still able to make a correct prediction with high probability.

IV. PROVABLE ROBUSTNESS ANALYSIS

In this section, we provide the provable robustness analysis for our robust masking defense. For any clean image \mathbf{x} and a given model \mathcal{M} , we will determine whether the attacker can bypass the robust masking defense, *with the knowledge of our defense*. Recall that our threat model only allows the adversarial patches to be within a fixed-size region, where the size of the region is a tunable security parameter. Given this threat model, we know that all the corrupted features will also be within a small window in the feature map space when using a model with a small receptive field.

Dilemma for the attacker. With the robust masking defense, we put the adversary in a dilemma. If the adversary wants to succeed in the attack, she needs to increase the class evidence of a wrong class. However, this increase of class

Algorithm 2 Provable analysis of robust masking

Input: Image \mathbf{x} , true class y , label set \mathcal{Y} , model \mathcal{M} , feature extractor \mathcal{F} , the set of sliding windows \mathcal{W} , and detection threshold T .

Output: Whether the image \mathbf{x} has provable robustness

```
1: procedure PROVABLEANALYSISMASKING
2:    $\bar{y} \leftarrow \mathcal{M}(\mathbf{x})$   $\triangleright$  Get the model prediction
3:   if  $\bar{y} \neq y$  then
4:     return False  $\triangleright$  Original prediction is incorrect
5:   end if
6:   for each  $y' \in \mathcal{Y}$  and  $y' \neq y$  do
7:      $\hat{\mathbf{u}}_y \leftarrow \text{CLIP}(\mathcal{F}(\mathbf{x}, y), 0, \infty)$   $\triangleright$  Get clipped local feature for true and target class
8:      $\hat{\mathbf{u}}_{y'} \leftarrow \text{CLIP}(\mathcal{F}(\mathbf{x}, y'), 0, \infty)$ 
9:     for each  $\mathbf{w} \in \mathcal{W}$  do
10:       $\delta \leftarrow \text{SUM}(((\mathbf{1} - \mathbf{w}) \odot (\hat{\mathbf{u}}_y - \hat{\mathbf{u}}_{y'})))$   $\triangleright$  Required minimum class evidence change
11:       $s_1 \leftarrow \text{NOWINDOW}(\hat{\mathbf{u}}_{y'}, \mathbf{w}, \delta)$   $\triangleright$  Cases for a potential successful attack
12:       $s_2 \leftarrow \text{BENIGNWINDOW}(\hat{\mathbf{u}}_y, \hat{\mathbf{u}}_{y'}, \mathbf{w}, \mathcal{W})$ 
13:       $s_3 \leftarrow \text{PARTMALWINDOW}(\hat{\mathbf{u}}_y, \hat{\mathbf{u}}_{y'}, \mathbf{w}, \mathcal{W})$ 
14:      if  $s_1 < T$  or  $s_2 > \delta$  or  $s_3 > \delta$  or  $\delta < 0$  then
15:        return False
16:      end if
17:    end for
18:  end for
19:  return True
20: end procedure

21: procedure NOWINDOW( $\hat{\mathbf{u}}_{y'}, \mathbf{w}, \delta$ )
22:    $s_1 \leftarrow \delta / (\text{SUM}((\mathbf{1} - \mathbf{w}) \odot \hat{\mathbf{u}}_{y'} + \delta))$ 
23:   return  $s_1$ 
24: end procedure

25: procedure BENIGNWINDOW( $\hat{\mathbf{u}}_y, \hat{\mathbf{u}}_{y'}, \mathbf{w}, \mathcal{W}$ )
26:    $\mathcal{W}' \leftarrow \{\mathbf{w}' | \mathbf{w}' \in \mathcal{W}, \text{SUM}(\mathbf{w}' \odot \mathbf{w}) = 0\}$ 
27:    $\mathbf{w}^* \leftarrow \arg \max_{\mathbf{w}' \in \mathcal{W}'} \text{SUM}(\mathbf{w}' \odot \hat{\mathbf{u}}_{y'})$ 
28:    $t \leftarrow \text{SUM}(\mathbf{w}^* \odot \hat{\mathbf{u}}_{y'})$ 
29:    $s_2 \leftarrow \text{SUM}(\mathbf{w}^* \odot \hat{\mathbf{u}}_y)$ 
30:   return  $s_2$ 
31: end procedure

32: procedure PARTMALWINDOW( $\hat{\mathbf{u}}_y, \hat{\mathbf{u}}_{y'}, \mathbf{w}, \mathcal{W}$ )
33:    $\mathcal{W}' \leftarrow \{\mathbf{w}' | \mathbf{w}' \in \mathcal{W}, \text{SUM}(\mathbf{w}' \odot \mathbf{w}) > 0\}$ 
34:    $\mathbf{w}^* \leftarrow \arg \max_{\mathbf{w}' \in \mathcal{W}'} \text{SUM}(\mathbf{w}' \odot \hat{\mathbf{u}}_y \odot (\mathbf{1} - \mathbf{w}'))$ 
35:    $s_3 \leftarrow \text{SUM}(\mathbf{w}^* \odot \hat{\mathbf{u}}_y \odot (\mathbf{1} - \mathbf{w}'))$ 
36:   return  $s_3$ 
37: end procedure
```

evidence will trigger our detection and masking mechanism. If the required minimum increase in malicious class evidence is large enough to trigger the detection, the adversary has little chance to succeed. We provide the pseudocode for the provable robustness analysis in Algorithm 2. Next, we will

explain Algorithm 2 and then prove that our approach provides provable robustness in Theorem 1.

Effect of clipping. To start with, we return `False` if the clean image \mathbf{x} cannot be correctly classified. Next, we iterate over all possible target classes to derive provable robustness for the untargeted attack. For each target class, we first get the clipped local feature for the true class and the target class. We always clip negative feature values to zero and leave positive values unchanged. If the feature is confidence tensor or prediction tensor, the feature values are already positive only. If the feature is logits, negative values do not contribute much to the clean image prediction but can be abused by the attacker to reduce the class evidence of the true class. Putting this constraint improves our robust accuracy.

Analyzing masking. The main analysis is in the inner for loop. We examine every possible window in the feature space. For each possible malicious window \mathbf{w} , we first ignore the elements within this window with the operation $(\mathbf{1} - \mathbf{w}) \odot (\cdot)$ and calculate the sum of the difference between two local feature tensors $\hat{\mathbf{u}}_y, \hat{\mathbf{u}}_{y'}$. The result δ is the minimum class evidence difference the adversary has to achieve by controlling the content within its malicious window \mathbf{w} for a successful attack. Since we have clipped negative feature values to zeros, the adversary only has two ways to attain this difference: 1) increase the class evidence of the target class within the small window \mathbf{w} it can control; 2) fool the detector to output a wrong window \mathbf{w}^* and zero out the class evidence of the true class within $\mathbf{w}^* \neq \mathbf{w}$. Based on this observation, we can prove the following theorem.

Theorem 1. *If Algorithm 2 returns `True` for a given image, our defense in Algorithm 1 can always make a correct prediction on the input image.*

Proof. For each possible malicious window \mathbf{w} , there are four possible cases for the output window \mathbf{w}^* of the `DETECT` sub-procedure, and we will discuss the condition for the potentially successful attack in each case.

- 1) *Case I: no suspicious window detected.* The attack succeeds only when the required minimum increase of the target class evidence δ does not exceed the detection threshold. If this condition is satisfied (i.e., $s_1 < T$), the algorithm returns `False`.
- 2) *Case II: a benign window is incorrectly detected.* In this case, the detected window \mathbf{w}^* satisfies $\text{SUM}(\mathbf{w}^* \odot \mathbf{w}) = 0$ (i.e., \mathbf{w}^* does not overlap with malicious window \mathbf{w}). We calculate the sum of target class evidence and true class evidence within the benign window \mathbf{w}^* to be t and s_2 , respectively. Since our defense will incorrectly zero out features within \mathbf{w}^* , the adversary achieves a difference of $s_2 - t$. Moreover, the adversary can also increase the malicious class evidence in its malicious window \mathbf{w} to t , and total class evidence achieved is $s_2 - t + t = s_2$. If $s_2 > \delta$, the attack might succeed, and the algorithm returns `False`. Note that the increase of malicious evidence within the malicious window \mathbf{w}

cannot be larger than t ; otherwise, the malicious window instead of the benign window will be detected.

- 3) *Case III: the malicious window is partially detected.* In this case, the detected window \mathbf{w}^* partially overlaps with the malicious window \mathbf{w} , or $\text{SUM}(\mathbf{w}^* \odot \mathbf{w}) > 0$. Following a similar reasoning as in *Case II*, the adversary can achieve a difference of $s = \text{SUM}(\mathbf{w}^* \odot \hat{\mathbf{u}}_y \odot (\mathbf{1} - \mathbf{w}))$ for each possible partially overlapped window \mathbf{w}^* . We output the largest s as s_3 , and return `False` if $s_3 > \delta$.
- 4) *Case IV: the malicious window is perfectly detected.* In this case, we have $\mathbf{w} = \mathbf{w}^*$. The attack can succeed only when feature masking will cause prediction change, or $\delta < 0$.

Algorithm 2 will check all possible malicious windows $\mathbf{w} \in \mathcal{W}$ for all possible target classes. If one of the conditions in the four cases is satisfied, the algorithm will return `False`. On the other hand, if the algorithm returns `True` instead of `False` after checking all possible malicious windows and target classes, this means our defense on this clean image has provable robustness against any possible patch and can always make a correct prediction. \square

V. EVALUATION

In this section, we provide a comprehensive evaluation of the proposed defense mechanism. We report the provable robust accuracy of our defense on a 10-class subset of ImageNet (called ImageNette [27]), the entire 1000-class ImageNet [24], and CIFAR-10 [28] for various patch sizes. We instantiate our defense with multiple different convolutional networks with small receptive fields and compare the results with previous defenses [18], [21], [22]. We also provide a detailed analysis of our defense performance with different parameters.

A. Experiment Setup

Datasets. We report our main provable robustness results on ImageNette [27], ImageNet [24] and CIFAR-10 [28] datasets. ImageNette and ImageNet images are in high resolution and will be resized and cropped to 224×224 or 299×299 before being fed into different models while CIFAR-10 images have a lower resolution of 32×32 . ImageNette is a 10-class subset of the large ImageNet dataset, we will provide a detailed analysis of different defense parameters on this smaller dataset. We include more details on these three datasets in Appendix A.

Models. As discussed in Section III-C, we have two general ways to build a network with small receptive fields. In our evaluation, we instantiate the first approach using a de-randomized smoothed ResNet (DS-ResNet) [22], and the second approach using BagNet [25]. The DS-ResNet [22] takes a rectangle pixel patch, or a pixel band, as the input of its base model and uses prediction majority voting for the ensemble prediction. In contrast, our defense uses *robust masking* for aggregation. The BagNet [25] architecture replaces a fraction of 3×3 convolution kernels of ResNet-50 with 1×1 kernels to reduce the receptive field size. It was originally

TABLE III
DEFAULT DEFENSE PARAMETERS FOR MASK-BN AND MASK-DS

| Setting | Feature | Parameters |
|-------------------------|----------------------------|-------------------------|
| Mask-BN on ImageNet(te) | BagNet-17 logits | $c_l = 0, c_h = \infty$ |
| Mask-BN on CIFAR-10 | BagNet-17 logits | $T = 0.0$ |
| Mask-DS on ImageNet | DS-25-ResNet-50 prediction | $c_l = 0$ |
| Mask-DS on ImageNette | DS-25-ResNet-50 confidence | $c_h = 1$ |
| Mask-DS on CIFAR-10 | DS-4-ResNet-18 confidence | $T = 0.0$ |

proposed in the context of interpretable machine learning while we use this model for provable robustness against adversarial patch attacks. We analyze performance of ResNet-50, BagNet-33, BagNet-17, BagNet-9, and a DS-ResNet with a band size of 25 (DS-25-ResNet-50). These 5 models have a similar network structure but have different receptive fields of 483×483 , 33×33 , 17×17 , 9×9 , and 25×299 , respectively. For CIFAR-10, we additionally include a DS-ResNet with a band size of 4 (DS-4-ResNet-18). We either use the pre-trained models available in [36]–[38] or retrain the models [36]–[38] pre-trained on ImageNet. We include more details of models in Appendix A.

Attacks. For ImageNette and ImageNet, we analyze our defense performance against a single adversarial patch that takes up 1%, 2%, or 3% pixels of the images. For CIFAR-10, we report results for a patch consisting of 0.4% or 2.4% of the image pixels. We use an empirical analysis to show the limitation of undefended vanilla models. For this analysis, we formulate the LaVAN [14] attack as a white-box untargeted attack due to its effectiveness. Due to computational constraints, we only consider a random location for each image in our empirical evaluation, which is a similar approach used in the LaVAN paper [14]. We empirically find that attacks with a random location are effective against undefended vanilla models. We note that our provable robustness result provides a bound against any adversarial patch attack, including an adaptive white-box attacker that tries all possible locations for an adversarial patch.

Defenses. We report the defense performance for our robust masking defense with BagNet (Mask-BN) and with a DS-ResNet (Mask-DS) on ImageNette, ImageNet, and CIFAR-10 datasets. We also compare with the existing Clipped BagNet (CBN) [21], De-randomized Smoothing (DS) [22] and Interval Bound Propagation based certified defense (IBP) [18]. The default parameters of our defense are listed in Table III. For previous defenses, we use the best parameters reported in the original papers.

Determining the window size. As introduced in Equation 2, the window size can be computed as $w = \lceil (p + r - 1) / s \rceil$. For the network architectures [36], [37] used in this paper, we have $s = 8$ for BagNet and $s = 1$ for DS-ResNet.

B. Provable Robustness Results

In this subsection, we report our main evaluation results for provable robustness. *Clean accuracy* refers to the classification accuracy on the clean validation images, and *adversar-*

TABLE IV
CLEAN AND EMPIRICAL ADVERSARIAL ACCURACY FOR UNDEFENDED MODELS

| Dataset | ImageNette | | | | | | ImageNet | | | | | | CIFAR-10 | | | |
|----------|------------|------|-----------|------|-----------|------|-----------|------|-----------|------|-----------|------|-------------|------|-------------|------|
| | 1% pixels | | 2% pixels | | 3% pixels | | 1% pixels | | 2% pixels | | 3% pixels | | 0.4% pixels | | 2.4% pixels | |
| Accuracy | clean | adv. | clean | adv. | clean | adv. | clean | adv. | clean | adv. | clean | adv. | clean | adv. | clean | adv. |
| ResNet | 99.6 | 47.3 | 99.6 | 14.9 | 99.6 | 4.0 | 76.1 | 11.7 | 76.1 | 2.8 | 76.1 | 0.5 | 97.0 | 83.4 | 97.0 | 38.2 |
| BagNet | 95.8 | 39.1 | 95.8 | 11.7 | 95.8 | 2.9 | 58.8 | 8.4 | 58.8 | 3.8 | 58.8 | 2.0 | 86.7 | 35.8 | 86.7 | 0.7 |

TABLE V
CLEAN AND PROVABLE ROBUST ACCURACY FOR DIFFERENT DEFENSES

| Dataset | ImageNette | | | | | | ImageNet | | | | | | CIFAR-10 | | | |
|----------|------------------------------|-------------|-------------|-------------|-------------|-------------|-------------|-------------|-------------|-------------|-------------|-------------|-------------|-------------|-------------|-------------|
| | 1% pixels | | 2% pixels | | 3% pixels | | 1% pixels | | 2% pixels | | 3% pixels | | 0.4% pixels | | 2.4% pixels | |
| Accuracy | clean | adv. | clean | adv. | clean | adv. | clean | adv. | clean | adv. | clean | adv. | clean | adv. | clean | adv. |
| Mask-BN | 93.0 | 87.6 | 92.4 | 85.2 | 91.7 | 81.6 | 53.1 | 19.9 | 51.9 | 14.4 | 50.7 | 9.8 | 79.5 | 58.6 | 76.2 | 37.2 |
| Mask-DS | 91.2 | 83.7 | 90.7 | 81.0 | 90.2 | 78.3 | 39.1 | 21.4 | 37.6 | 17.7 | 36.4 | 14.8 | 82.6 | 72.1 | 80.0 | 62.2 |
| IBP [18] | computationally inapplicable | | | | | | | | | | | | 65.8 | 51.9 | 47.8 | 30.8 |
| CBN [21] | 94.9 | 74.6 | 94.9 | 60.9 | 94.9 | 45.9 | 49.5 | 13.4 | 49.5 | 7.1 | 49.5 | 3.1 | 84.2 | 44.2 | 84.2 | 9.3 |
| DS [22] | 92.1 | 82.3 | 92.1 | 79.1 | 92.1 | 75.7 | 44.4 | 17.7 | 44.4 | 14.0 | 44.4 | 11.2 | 83.9 | 68.9 | 83.9 | 56.2 |

ial/robust accuracy refers to the model accuracy on adversarial images from the validation set.

Vanilla models are vulnerable to adversarial patch attacks.

We report the clean and empirical adversarial accuracies of undefended vanilla ResNet and BagNet in Table IV. We attack these models with the untargeted LaVAN attack at one random location for each image. We report the empirical attack results for the entire validation set for ImageNette and CIFAR-10 as well as 2500 randomly selected validation images from ImageNet.⁴ We can see both vanilla ResNet and BagNet are vulnerable to adversarial patch attacks; a small patch consisting of only 3% pixels can degrade the model accuracy close to zero on ImageNet. Therefore, it is necessary to defend against such attacks. Note that DS-ResNet was proposed in [22] as a defense model; we report the result of vanilla DS-ResNet (DS) in Table V instead of Table IV.

Robust Masking significantly improves model robustness with a high clean accuracy.

We report our main provable robustness results, *against all possible adversaries*, in Table V. Our results for Mask-BN and Mask-DS demonstrate that our defense leads to high provable robust accuracy across datasets and models. For a 2% pixel patch, Mask-BN achieves 85.2% provable accuracy on ImageNette and 14.4% on ImageNet while Mask-DS has 81.0% provable accuracy on ImageNette and 17.7% on ImageNet. For a 2.4% pixel patch on CIFAR-10, Mask-BN and Mask-DS achieve a provable robust accuracy of 37.2% and 62.2%, respectively.

Simultaneously, our defenses retain high clean accuracy. For a 2% pixel patch, Mask-BN has 92.4% clean accuracy on ImageNette and 51.9% on ImageNet while Mask-DS achieves 90.7% clean accuracy on ImageNette and 37.6% on ImageNet. For CIFAR-10, Mask-BN and Mask-DS have a high clean accuracy of 76.2% and 80.0%. The clean accuracy drop

⁴Provable results of ImageNet are evaluated on the entire validation set.

of Mask-BN and Mask-DS on ImageNette compared with undefended ResNet is within 10%. The accuracy drop of Mask-BN from the undefended BagNet is only around 3%. We can also see a similar moderate clean accuracy drop for the other two datasets. We note that robust masking uses a different window size for different patch sizes, and therefore the clean accuracy for different patches varies slightly.

Robust Masking achieves higher provable accuracy than all previous defenses.

We compare our defense performance with existing defenses across three datasets. On ImageNette, our Mask-BN achieves the best provable accuracy for three different patch sizes. Its clean accuracy is slightly lower than CBN, but we note that our provable robust accuracy is much higher, especially when the patch size is large. When the patch takes up 3% image pixels, the provable accuracy of Mask-BN is 35.7% higher than that of CBN while the clean accuracy is only 3.2% lower. Our Mask-BN also outperforms DS in terms of clean accuracy and provable accuracy. Mask-DS has better provable accuracy but lower clean accuracy compared with DS and CBN. We do not report results for IBP on ImageNette and ImageNet because IBP is too computationally expensive to scale to high-resolution images.

On ImageNet, our defenses also achieve the best performance. Both Mask-BN and Mask-DS have a much higher provable accuracy than CBN. The provable robustness of Mask-BN and Mask-DS is either comparable or moderately higher than DS⁵, but we achieve significantly higher clean accuracy with Mask-BN (51.9% for Mask-BN at 2% pixels, compared to 44.4% for DS).

For CIFAR-10, both Mask-BN and Mask-DS defenses sig-

⁵The provable robust accuracy for 2% pixel patches reported in DS paper [22] is 14.5%, but that result is for a subset of 1000 images. We successfully reproduced their results of 14.5% and scaled the evaluation to the entire validation set, which resulted in a provable accuracy of 14.0%.

TABLE VI
EMPIRICAL ACCURACY OF UNDEFENDED VANILLA MODELS

| | Clean | 1% pixels adv. | 2% pixels adv. | 3% pixels adv. |
|-----------|-------|----------------|----------------|----------------|
| ResNet-50 | 99.6% | 47.3% | 14.9% | 4.0% |
| BagNet-33 | 97.4% | 27.0% | 4.8% | 1.1% |
| BagNet-17 | 95.8% | 39.1% | 11.7% | 2.9% |
| BagNet-9 | 92.7% | 26.8% | 14.8% | 3.8% |

TABLE VII
INVARIANCE OF BAGNET-17 PREDICTIONS TO FEATURE MASKING

| Window size | 0×0 | 2×2 | 4×4 | 6×6 | 8×8 |
|---------------------|-------|-------|-------|-------|-------|
| Masked accuracy | 95.8% | 95.8% | 95.7% | 95.6% | 95.4% |
| % images | 4.3% | 5.3% | 6.6% | 8.1% | 9.8% |
| % windows per image | 0% | 0.05% | 0.2% | 0.4% | 0.7% |

nificantly outperform IBP in terms of clean accuracy and provable accuracy. Our Mask-DS achieves the best provable robustness compared to all prior works including CBN and DS, but its clean accuracy is slightly lower than DS. Mask-BN does not perform as well on CIFAR-10 because we find that lower resolution images in CIFAR-10 affect the performance of the BagNet architecture. We expect that the performance of the approach will improve with better architectures. We note that CBN relies only on BagNet as opposed to our approach of robust masking. CBN is thus very fragile on CIFAR-10 due to the lower resolution images, achieving the worst provable performance in prior works.

Takeaways. Our evaluation shows the effectiveness of our proposed defenses, achieving state-of-the-art provable robustness on all three datasets. We find that BagNet-based defenses (Mask-BN and CBN) perform well on ImageNette and ImageNet but are fragile on CIFAR-10 due to its low image resolution. Meanwhile, De-randomized Smoothing based defenses (Mask-DS and DS) perform better on CIFAR-10. This shows that while the *robust masking* defense always improves robustness, its impact varies depending on the choice of model and dataset.

C. Detailed Analysis of Robust Masking

In this subsection, we use ImageNette to analyze the performance of robust masking under different defense parameters. We will only report results for Mask-BN when the observations from Mask-BN and Mask-DS are very similar. We include the results for CIFAR-10 in Appendix D.

Undefended vanilla models. We report the clean and adversarial accuracy of vanilla models with different receptive field sizes in Table VI. The clean accuracy of BagNet decreases as its receptive field becomes smaller since each local feature receives less information. Furthermore, we observe that all undefended vanilla models are vulnerable to adversarial patch attacks; a patch consisting of only 3% pixels can achieve an attack success rate higher than 96% across all models, which makes our defense necessary.

Prediction invariance of vanilla models to feature masking. In our *robust masking* defense, we detect and mask corrupted

TABLE VIII
EFFECT OF LOGITS CLIPPING VALUES ON VANILLA MODELS

| (c_l, c_h) | $(-\infty, \infty)$ | $(0, \infty)$ | $(0, 50)$ | $(0, 15)$ | $(0, 5)$ |
|--------------|---------------------|---------------|-----------|-----------|----------|
| ResNet-50 | 99.6% | 99.5% | 99.5% | 99.5% | 99.0% |
| BagNet-33 | 97.4% | 97.2% | 97.1% | 95.8% | 93.4% |
| BagNet-17 | 95.8% | 95.1% | 94.3% | 92.2% | 88.5% |
| BagNet-9 | 92.7% | 90.1% | 89.1% | 87.3% | 81.7% |

TABLE IX
EFFECT OF RECEPTIVE FIELD SIZES ON PROVABLE ROBUST ACCURACY

| Patch size | 1% pixels | | 2% pixels | | 3% pixels | |
|------------|-----------|-------|-----------|-------|-----------|-------|
| Accuracy | clean | adv. | clean | adv. | clean | adv. |
| BagNet-33 | 94.7% | 87.8% | 93.9% | 84.5% | 93.0% | 79.6% |
| BagNet-17 | 93.0% | 87.6% | 92.4% | 85.2% | 91.7% | 81.6% |
| BagNet-9 | 88.0% | 82.8% | 87.4% | 80.5% | 86.4% | 77.4% |

features. If the model can make correct predictions from the aggregation of the remaining features, we can recover the correct prediction. Therefore, we first analyze the prediction invariance of vanilla models to partial feature masking. We take BagNet-17, which has $26 \cdot 26$ local features, for the case study. We mask out features within a set of sliding windows of different sizes and record the prediction from the remaining features. We report the averaged accuracy for all possible masked feature tensors (masked accuracy), the percentage of images for which at least one masked prediction is incorrect (% images), and the percentage of masks that will cause prediction change for each image (% windows per image). As shown in Table VII, the overall averaged masked accuracy is high, and the percentage of images and windows for which the prediction changes is low. Note that when there is at least one masked window that could cause a prediction change, the adversary can simply put a patch at the corresponding region of the input image and have a trivially successful untargeted attack. The small fraction of images with prediction changes enables us to achieve a high provable robustness while maintaining clean accuracy by recovering correct predictions. We find that similar observations hold for other models.

Effect of clipping on vanilla models. The default clipping values for Mask-BN are $c_l = 0, c_h = \infty$ when the feature type is the logits tensor. We vary the clipping value for the local logits for ResNet and BagNet to determine how the clean accuracy changes, and the results are shown in Table VIII. We find that clipping the negative values only slightly affects the clean accuracy. When we decrease the positive clipping value c_h , the clean accuracy of the model also decreases. We notice that models with smaller receptive fields are more sensitive to clipping. This is because models with small receptive fields only have a small number of correct local predictions. The corresponding correctly predicted local logits have to use large logit values to dominate the global prediction, which leads to the sensitivity to clipping. As shown in Figure 3, the logits of the adversarial images tend to have large values. If we set c_h to the largest clean logits value, we will not affect the clean

TABLE X
PROVABLE ACCURACY AND FAILURE CASE BREAKDOWN OF BAGNET-17
WITH DIFFERENT DETECTION THRESHOLDS

| | Clean | Provable | FP | Case I / IV | Case II | Case III |
|-------|-------|----------|-------|-------------|---------|----------|
| T-0.0 | 92.4% | 85.2% | 100% | 0.2% | 2.9% | 6.8% |
| T-0.2 | 92.7% | 82.9% | 39.9% | 8.6% | 0.4% | 3.2% |
| T-0.4 | 94.3% | 69.2% | 3.2% | 25.2% | 0% | 0.6% |
| T-0.6 | 94.9% | 42.3% | 0.3% | 52.7% | 0% | 0.1% |
| T-0.8 | 95.1% | 10.4% | 0% | 84.7% | 0% | 0% |
| T-1.0 | 95.1% | 0% | 0% | 95.1% | 0% | 0% |

TABLE XI
EFFECT OF FEATURE TYPES ON MASK-BN

| Patch size | 1% pixels | | 2% pixels | | 3% pixels | |
|------------|-----------|-------|-----------|-------|-----------|-------|
| Accuracy | clean | adv. | clean | adv. | clean | adv. |
| Logits | 93.0% | 87.6% | 92.4% | 85.2% | 91.7% | 81.6% |
| Confidence | 84.6% | 77.9% | 84.2% | 75.1% | 83.4% | 71.8% |
| Prediction | 80.3% | 72.4% | 80.2% | 69.6% | 79.7% | 66.6% |

accuracy and can improve the empirical robustness against the adversarial patch. We note that setting c_h to a large real number *will not affect the provable robustness compared with setting $c_h = \infty$* . When features correspond to confidence or prediction values, we do not suggest any additional clipping since those values are already bounded between 0 and 1.

Effect of receptive field sizes on defended models. We report clean accuracy and provable robust accuracy of our defense for BagNet-33, BagNet-17, and BagNet-9, which have a receptive field of 33×33 , 17×17 , and 9×9 , respectively, against different patch sizes in Table IX. As shown in the table, a model with a larger receptive field has better clean accuracy. However, a larger receptive field results in a larger fraction of corrupted features and thus a larger gap between clean accuracy and provable robust accuracy. We can see that though BagNet-33 has a higher clean accuracy than BagNet-17, its gap between clean accuracy and provable robust accuracy is larger, which results in a similar or slightly poorer provable robust accuracy compared with BagNet-17.

Effect of the detection threshold on defended models. We study the model performance of BagNet-17 against a 2% pixel patch as we change the detection threshold T from 0.0 to 1.0. A threshold of zero means our detection will always return a suspicious window even if the input is a clean image while a threshold of one means no detection at all. We report the clean accuracy (Clean), provable robust accuracy (Provable), and false positive (FP) rates for detection of suspicious windows on clean images in the left part of Table X. As we increase the detection threshold T , we reduce the FP rate for detection of a suspicious window in clean images, at the cost of making it easier for an adversarial patch to succeed via *Case I* (no suspicious window detected). *However, we note that FP in the detection phase for clean images have minimal impact on the clean accuracy because our models are invariant to feature masking, as already shown in Table VII.* Thus, we find $T = 0$ to be the best choice for this dataset (even with an FP

TABLE XII
EFFECT OF FEATURE TYPES ON MASK-DS

| Patch size | 1% pixels | | 2% pixels | | 3% pixels | |
|------------|-----------|-------|-----------|-------|-----------|-------|
| Accuracy | clean | adv. | clean | adv. | clean | adv. |
| Logits | 91.6% | 78.0% | 91.1% | 70.5% | 90.6% | 63.7% |
| Confidence | 91.2% | 83.7% | 90.7% | 81.0% | 90.2% | 78.3% |
| Prediction | 91.4% | 83.2% | 90.3% | 80.2% | 89.8% | 77.7% |

TABLE XIII
PER-IMAGE INFERENCE TIME OF DIFFERENT MODELS ON IMAGENETTE

| Model | ResNet-50 | BagNet-17 | DS-25-ResNet | Mask-BN | Mask-DS |
|-------|-----------|-----------|--------------|---------|---------|
| Time | 16.5ms | 19.5ms | 378.0ms | 21.8ms | 379.1ms |

of 100%); it results in the highest provable robust accuracy of 85.2% while only incurring a 2.7% clean accuracy drop compared to $T = 1$.

Breakdown of provable analysis on defended models. We study the failure cases of our provable analysis and report the results in the right part of Table X. We do not consider incorrectly classified clean images (that return `False` in Line 4 of Algorithm 2, corresponding to 4.9% of all clean images in this setting). Note that each image might be attacked via multiple failure cases introduced in Section IV. We only count the first found failure case; if we find that an image can be attacked via *Case I*, we will not consider whether it can be attacked via *Case II or III*. We merge *Case I* and *Case IV* in the table because when the condition of *Case IV* is satisfied ($\delta < 0$), the condition of *Case I* will always be satisfied ($s_1 = \delta / \text{SUM}((1 - \mathbf{w}) \odot \hat{\mathbf{u}}_{y'} + \delta) < 0 \leq T$). As shown in Table X, when we set the detection threshold to zero, the majority of failure cases come from a partially detected malicious window (*Case III*: 6.8%). When the detection threshold increases, *no suspicious windows detected (Case I)* becomes the major failure case.

Effect of using different feature types for defended models. In this analysis, we study the performance of the robust masking defense when using different types of features, namely logits, confidence values, and predictions. The results for BagNet-17 with different features are reported in Table XI. As shown in the table, using logits as the feature type has a much better performance than confidence and prediction in terms of clean accuracy and provable accuracy. The main reason for this observation is that BagNet is trained with logits aggregation. Our additional analysis shows that BagNet does not have high model performance when trained with confidence or prediction aggregation; therefore, we use logits as our default feature type for Mask-BN. Interestingly, Mask-DS exhibits a different behavior. As shown in Table XII, Mask-DS works better when we use prediction or confidence as feature types due to its different training objectives. In conclusion, the performance of different feature types largely depends on the training objective of the network with small receptive fields, and should be appropriately optimized to determine the best defense setting.

Model inference efficiency. As discussed in Section III-C,

using an ensemble model (e.g., DS-ResNet) is computationally expensive compared with using small convolution kernels in conventional convolutional networks (e.g., BagNet). In Table XIII, we report the per-image inference time of different models on the ImageNette validation set. As shown in the table, the inference time of BagNet-17 (19.5ms) is close to that of ResNet (16.5ms) while DS-25-ResNet needs a much longer time (378.0ms). Therefore, we suggest using small convolution kernels to build models with small receptive fields when the two approaches have similar defense performance. Moreover, we note that our *robust masking* is efficient, only incurring a ~ 2 ms defense overhead on each ImageNette validation image.

VI. DISCUSSION

In this section, we will show that our defense is a generalization of previous provable defenses and discuss future research directions pertaining to our defense.

A. Generalization of Previous Provable Defenses

Clipped BagNet (CBN). CBN [21] proposes clipping the local logits tensor with function $\text{CLIP}(\mathbf{u}) = \tanh(0.05 \cdot \mathbf{u} - 1)$ to improve the robustness of BagNet [25]. Since the range of $\tanh(\cdot)$ is bounded by $(-1, 1)$, the adversary can achieve at most $2k$ difference in clipped logits values between the true class and any other class, where k is the number of corrupted local logits due to the adversarial patch. In its provable analysis, CBN calculates the difference between the sum of unaffected logits values for the predicted class and the second predicted class as δ ; if $\delta > 2k$, CBN certifies the robustness of the input clean image. To reduce our Mask-BN defense to CBN, we can set our feature type to logits, the detection threshold to $T = 1$, and adjust the clipping values c_l and c_h or the clipping function $\text{CLIP}(\cdot)$. Our evaluation shows that our defense significantly outperforms CBN across three different datasets. One major reason for this performance difference is the use of sub-optimal clipping function in CBN (i.e., $\tanh(\cdot)$). Our analysis shows that the negative values contribute little to the prediction but can be abused by the adversary; thus, this clipping design leads to a loose bound.

De-randomized Smoothing (DS). DS [22] trains a ‘smoothed’ classifier on image pixel patches and computes the predicted class as the class with the largest count in local predictions made from all pixel patches (i.e., majority voting). The provable robustness analysis of DS only considers the largest and second-largest counts of local predictions. If the gap between the two largest counts is larger than $2k$, where k is the upper bound of the number of corrupted predictions, DS certifies the robustness of the image. When we set the feature type to prediction and detection threshold to $T = 1$, we can reduce Mask-DS to DS. Note that averaging all one-hot encoded local predictions gives the same global prediction as majority voting. Two major reasons lead to the worse provable performance of DS. First, the certification process of DS discards the spatial information of each prediction while our robust masking defense utilizes the spatial information that all corrupted features are within a small window in the feature space. Second, DS

needs to use $2k$ as the threshold for certification while the maximum value of s_2 and s_3 in Algorithm 2 is only k when we set the feature type to prediction. Further details of these claims are in Appendix E. In summary, our robust masking can derive a tighter bound than DS, which is supported by results in Section V.

B. Future Work

Improve the design and training of networks with small receptive fields. The foundation of our defense is convolutional networks with a small receptive field, and we use two such instances via BagNet [25] and DS-ResNet [22]. Our current defense performance is largely constrained by the clean accuracy of BagNet and DS-ResNet, despite the fact that our defense framework is compatible with any network with small receptive fields. We hope that our work inspires the design of novel network architectures that have a small receptive field while maintaining state-of-the-art clean accuracy, which would further boost the performance of our defense. We note that we do not use adversarial training [2], [5], [39] in our defense because we want to have a model with high clean accuracy, which is difficult for state-of-the-art algorithms [39].

Use a “soft” constraint via quantitatively bounding the contribution of each pixel. In our work, we use a hard constraint to limit the number of corrupted features due to an adversarial patch to provide provable robustness. However, as each local feature focuses exponentially more on the center of its receptive field (more explanations in Appendix C), pixels far away from the center of the receptive field only have a limited influence on the local feature. This behavior can be regarded as a “soft” limitation of the receptive field size. If we can quantitatively bound the influence of each pixel on the local feature, we can have a more fine-grained bound on the robust accuracy. We hope that our work inspires future research on the relationship between receptive field sizes and model robustness.

Explore alternative secure feature aggregation approaches. We present *robust masking* to compute robust predictions from partially corrupted features, and we note that it is just a single instance of our broader defense framework. Our defense framework turns the problem of designing an adversarial patch defense into a robust aggregation problem, i.e., *how can we make a robust prediction from a partially corrupted feature tensor?* Techniques from robust statistics such as clipping, median, truncated mean as well as differential privacy [40] can also be incorporated in our framework. We provide an empirical analysis of alternative aggregation approaches in Appendix F. Interestingly, we find that ResNet can also benefit from secure aggregation techniques such as clipping and median despite its large receptive fields. We believe this is due to the limited influence of an adversarial patch far away from the receptive field center of the local feature (Appendix C), and this observation further motivates our future work on the “soft” constraint on the size of the receptive field. We note that our defense framework is compatible with alternative

aggregation techniques; we only need to tailor the provable analysis algorithm for different aggregation approaches.

VII. RELATED WORK

A. Localized Adversarial Perturbations

Most adversarial example research focuses on L_p -norm bounded perturbations added to the entire input. In contrast, localized adversaries have received much less attention. The adversarial patch attack was introduced by Brown et al. [13] and focused on physical and universal patches to induce targeted misclassification. Attacks in the real-world can be realized by attaching a patch to the victim object. A follow-up paper on Localized and Visible Adversarial Noise (LaVAN) attack [14] aimed at inducing targeted misclassification in the digital domain. Both of these papers operated in the white-box threat model, with access to the internals of the classifier under attack. PatchAttacker [41], on the other hand, proposed a reinforcement learning-based targeted attack to generate an adversarial patch in a black-box setting. In this paper, we focus on provable defenses against any white-box attacks such as LaVAN, which we find to be the most effective attack.

Localized patch attacks against object detection [42], [43], semantic segmentation models [44] as well as training-time poisoning attacks using localized triggers [45], [46] have been proposed. Our threat model in this paper focuses on attacks against image classification models at test time, but we expect that our defense can be generalized to the above settings.

Eykholt et al. [15] demonstrated a physical-world attack that attached small stickers to a stop sign for fooling traffic sign classification; this attack is already considered in our threat model. Sharif et al. [47] proposed an eyeglass attack against real-world face recognition, in which the adversary wears adversarial glasses to evade being recognized or to impersonate another individual. The location of the perturbation is constrained to be on the eyeglasses; an interesting direction of future work is to tailor our defense framework for this attack.

B. Adversarial Patch Defenses

Several defenses have been proposed to mitigate the adversarial patch attack. Digital Watermark (DW) [16] generated a saliency map to detect important pixels and then tried to remove adversarial pixels. However, its detection mechanism is vulnerable to the Backward Pass Differentiable Approximation (BPDA) attack [11], which could trick the model into removing benign pixels [18]. Local Gradient Smoothing (LGS) [17] smoothed the suspicious areas of the images to neutralize the effect of the adversarial pixels, but has been bypassed via incorporating the smoothing function into the attack optimization objective [18].

Observing the ineffectiveness of DW and LGS against an adaptive attacker, Chiang et al. [18] proposed the first certified defense against adversarial patch via Interval Bound Propagation (IBP) [19], [20] which traces the influence of adversarial pixels on the hidden representation of each layer and derives a bound for the certified prediction. Despite its

important theoretical contribution, the IBP defense has poor clean and provable robust accuracy, as shown in Table V. Zhang et al. [21] proposed to use clipped BagNet (CBN) to achieve provable robustness. We have shown that CBN is an instance of our general defense framework (Section VI-A), and our robust masking has a better defense performance (Section V-B). De-randomized Smoothing (DS) [22] proposed building a ‘smoothed’ classifier that outputs the class with the largest count from local predictions on all small pixel patches. We have also shown that DS is an instance of our defense framework (Section VI-A), and our defense outperforms DS (Section V-B). The Minority Report (MR) [26] defense was proposed in concurrent work, where the defender puts a mask at all possible locations and extracts patterns from model predictions on all masked images to detect the adversarial attack. This method incurs a large computational cost by doing inference on all possible masked images and does not scale to ImageNet. Further, this defense only detects the presence of an attack, rather than recovering the correct prediction. This design allows the adversary to force the model to abstain from prediction while our model can always make correct predictions on certified images.

C. Receptive Fields of Convolutional Networks

Several works have studied the influence of the receptive field [25], [35], [48], [49] on the model performance in order to better understand the model behavior. BagNet [25] adopted the structure of ResNet-50 [23] but reduced the receptive field size by replacing 3×3 kernels with 1×1 kernels. BagNet-17 can achieve similar validation accuracy as AlexNet [32] on ImageNet [24] dataset when each feature only looks at a 17×17 pixel region. The small receptive field was used for better interpretability of model decisions in the original BagNet paper. In this work, we use the reduced receptive field size for the model robustness to adversarial patch attacks.

D. Other Adversarial Example Attacks and Defenses

Adversarial example attacks and defenses have been an extremely active research area over the past few years. Conventional adversarial attacks [1]–[4] craft adversarial examples that have a small L_p distance to normal examples but will induce model misclassification. Many empirical defenses [5]–[9] have been proposed to address the adversarial example vulnerability, but most of them can be easily bypassed by a strong adaptive attacker [10]–[12]. The fragility of the empirical defenses has inspired provable or certified defenses [19], [20], [50]–[54] as well as work on learning-theoretic bounds in the presence of adversaries [55]–[59]. In contrast, the focus of this paper is on localized adversarial patch attacks, and we refer interested readers to survey papers [60], [61] for a detailed exposition of adversarial examples.

VIII. CONCLUSION

In this paper, we propose a general provable defense framework called PatchGuard that mitigates localized adversarial patch attacks. We identify large receptive fields and insecure

aggregation approaches in conventional convolutional networks as the source of vulnerability to adversarial patches. To address these two problems, our defense reduces the size of the receptive field to limit the number of features corrupted by the adversary and further uses a *robust masking* defense to detect and mask the corrupted features for secure aggregation. Our defense achieves state-of-the-art provable robust accuracy on ImageNette, ImageNet, and CIFAR-10 datasets. We hope that our general defense framework will inspire further research to fully mitigate adversarial patch attacks.

REFERENCES

- [1] C. Szegedy, W. Zaremba, I. Sutskever, J. Bruna, D. Erhan, I. J. Goodfellow, and R. Fergus, "Intriguing properties of neural networks," in *2nd International Conference on Learning Representations (ICLR)*, 2014.
- [2] I. J. Goodfellow, J. Shlens, and C. Szegedy, "Explaining and harnessing adversarial examples," in *3rd International Conference on Learning Representations (ICLR)*, 2015.
- [3] N. Papernot, P. D. McDaniel, S. Jha, M. Fredrikson, Z. B. Celik, and A. Swami, "The limitations of deep learning in adversarial settings," in *IEEE European Symposium on Security and Privacy (EuroS&P)*, 2016, pp. 372–387.
- [4] N. Carlini and D. A. Wagner, "Towards evaluating the robustness of neural networks," in *2017 IEEE Symposium on Security and Privacy (S&P)*, 2017, pp. 39–57.
- [5] A. Madry, A. Makelov, L. Schmidt, D. Tsipras, and A. Vladu, "Towards deep learning models resistant to adversarial attacks," in *6th International Conference on Learning Representations (ICLR)*, 2018.
- [6] N. Papernot, P. D. McDaniel, X. Wu, S. Jha, and A. Swami, "Distillation as a defense to adversarial perturbations against deep neural networks," in *IEEE Symposium on Security and Privacy (S&P)*, 2016, pp. 582–597.
- [7] W. Xu, D. Evans, and Y. Qi, "Feature squeezing: Detecting adversarial examples in deep neural networks," in *25th Annual Network and Distributed System Security Symposium (NDSS)*, 2018.
- [8] D. Meng and H. Chen, "Magnet: A two-pronged defense against adversarial examples," in *Proceedings of the 2017 ACM SIGSAC Conference on Computer and Communications Security (CCS)*, 2017, pp. 135–147.
- [9] J. H. Metzen, T. Genewein, V. Fischer, and B. Bischoff, "On detecting adversarial perturbations," in *5th International Conference on Learning Representations (ICLR)*, 2017.
- [10] N. Carlini and D. A. Wagner, "Adversarial examples are not easily detected: Bypassing ten detection methods," in *Proceedings of the 10th ACM Workshop on Artificial Intelligence and Security (AISec@CCS)*, 2017, pp. 3–14.
- [11] A. Athalye, N. Carlini, and D. A. Wagner, "Obfuscated gradients give a false sense of security: Circumventing defenses to adversarial examples," in *Proceedings of the 35th International Conference on Machine Learning (ICML)*, 2018, pp. 274–283.
- [12] F. Tramer, N. Carlini, W. Brendel, and A. Madry, "On adaptive attacks to adversarial example defenses," *arXiv preprint arXiv:2002.08347*, 2020.
- [13] T. B. Brown, D. Mané, A. Roy, M. Abadi, and J. Gilmer, "Adversarial patch," in *Advances in neural information processing systems workshops (NeurIPS Workshops)*, 2017.
- [14] D. Karmon, D. Zoran, and Y. Goldberg, "LaVAN: Localized and visible adversarial noise," in *Proceedings of the 35th International Conference on Machine Learning (ICML)*, 2018, pp. 2512–2520.
- [15] K. Eykholt, I. Evtimov, E. Fernandes, B. Li, A. Rahmati, C. Xiao, A. Prakash, T. Kohno, and D. Song, "Robust physical-world attacks on deep learning visual classification," in *2018 IEEE Conference on Computer Vision and Pattern Recognition (CVPR)*, 2018, pp. 1625–1634.
- [16] J. Hayes, "On visible adversarial perturbations & digital watermarking," in *2018 IEEE Conference on Computer Vision and Pattern Recognition Workshops (CVPR Workshops)*, 2018, pp. 1597–1604.
- [17] M. Naseer, S. Khan, and F. Porikli, "Local gradients smoothing: Defense against localized adversarial attacks," in *IEEE Winter Conference on Applications of Computer Vision (WACV)*, 2019, pp. 1300–1307.
- [18] P.-Y. Chiang, R. Ni, A. Abdelkader, C. Zhu, C. Studor, and T. Goldstein, "Certified defenses for adversarial patches," in *8th International Conference on Learning Representations (ICLR)*, 2020.
- [19] S. Gowal, K. Dvijotham, R. Stanforth, R. Bunel, C. Qin, J. Uesato, R. Arandjelovic, T. A. Mann, and P. Kohli, "Scalable verified training for provably robust image classification," in *2019 IEEE/CVF International Conference on Computer Vision (ICCV)*, 2019, pp. 4841–4850.
- [20] M. Mirman, T. Gehr, and M. T. Vechev, "Differentiable abstract interpretation for provably robust neural networks," in *Proceedings of the 35th International Conference on Machine Learning (ICML)*, 2018, pp. 3575–3583.
- [21] Z. Zhang, B. Yuan, M. McCoyd, and D. Wagner, "Clipped bagnet: Defending against sticker attacks with clipped bag-of-features," in *3rd Deep Learning and Security Workshop (DLS)*, 2020.
- [22] A. Levine and S. Feizi, "(De)randomized smoothing for certifiable defense against patch attacks," *arXiv preprint arXiv:2002.10733*, 2020.

- [23] K. He, X. Zhang, S. Ren, and J. Sun, "Deep residual learning for image recognition," in *2016 IEEE Conference on Computer Vision and Pattern Recognition (CVPR)*, 2016, pp. 770–778.
- [24] J. Deng, W. Dong, R. Socher, L. Li, K. Li, and F. Li, "ImageNet: A large-scale hierarchical image database," in *2009 IEEE Computer Society Conference on Computer Vision and Pattern Recognition (CVPR)*, 2009, pp. 248–255.
- [25] W. Brendel and M. Bethge, "Approximating CNNs with bag-of-local-features models works surprisingly well on ImageNet," in *7th International Conference on Learning Representations (ICLR)*, 2019.
- [26] M. McCoyd, W. Park, S. Chen, N. Shah, R. Roggenkemper, M. Hwang, J. X. Liu, and D. Wagner, "Minority reports defense: Defending against adversarial patches," *arXiv preprint arXiv:2004.13799*, 2020.
- [27] fast.ai, "ImageNette: A smaller subset of 10 easily classified classes from imagenet," <https://github.com/fastai/imagenette>, 2020.
- [28] A. Krizhevsky, "Learning multiple layers of features from tiny images," <https://www.cs.toronto.edu/~kriz/learning-features-2009-TR.pdf>, 2009.
- [29] C. Szegedy, S. Ioffe, V. Vanhoucke, and A. A. Alemi, "Inception-v4, inception-resnet and the impact of residual connections on learning," in *Proceedings of the Thirty-First AAAI Conference on Artificial Intelligence (AAAI)*, 2017, pp. 4278–4284.
- [30] C. Szegedy, W. Liu, Y. Jia, P. Sermanet, S. Reed, D. Anguelov, D. Erhan, V. Vanhoucke, and A. Rabinovich, "Going deeper with convolutions," in *Proceedings of the IEEE conference on computer vision and pattern recognition (CVPR)*, 2015, pp. 1–9.
- [31] K. Simonyan and A. Zisserman, "Very deep convolutional networks for large-scale image recognition," in *3rd International Conference on Learning Representations (ICLR)*, 2015.
- [32] A. Krizhevsky, I. Sutskever, and G. E. Hinton, "ImageNet classification with deep convolutional neural networks," in *Advances in neural information processing systems (NeurIPS)*, 2012, pp. 1106–1114.
- [33] J. Kiefer, J. Wolfowitz *et al.*, "Stochastic estimation of the maximum of a regression function," *The Annals of Mathematical Statistics*, vol. 23, no. 3, pp. 462–466, 1952.
- [34] L. Bottou, F. E. Curtis, and J. Nocedal, "Optimization methods for large-scale machine learning," *SIAM Review*, vol. 60, no. 2, pp. 223–311, 2018.
- [35] A. Araujo, W. Norris, and J. Sim, "Computing receptive fields of convolutional neural networks," *Distill*, 2019, <https://distill.pub/2019/computing-receptive-fields>.
- [36] A. Levine and S. Feizi, "Code for the paper "(de)randomized smoothing for certifiable defense against patch attacks"," <https://github.com/alevine0/patchSmoothing>, 2020.
- [37] W. Brendel, "Pretrained bag-of-local-features neural networks," <https://github.com/wielandbrendel/bag-of-local-features-models>, 2020.
- [38] Torchvision, "torchvision.models," <https://pytorch.org/docs/stable/torchvision/models.html>, 2020.
- [39] T. Wu, L. Tong, and Y. Vorobeychik, "Defending against physically realizable attacks on image classification," in *8th International Conference on Learning Representations (ICLR)*, 2020.
- [40] C. Dwork and A. Roth, "The algorithmic foundations of differential privacy," *Foundations and Trends in Theoretical Computer Science*, vol. 9, no. 3-4, pp. 211–407, 2014.
- [41] C. Yang, A. Kortylewski, C. Xie, Y. Cao, and A. Yuille, "Patchattack: A black-box texture-based attack with reinforcement learning," *arXiv preprint arXiv:2004.05682*, 2020.
- [42] X. Liu, H. Yang, Z. Liu, L. Song, Y. Chen, and H. Li, "DPATCH: an adversarial patch attack on object detectors," in *Workshop on Artificial Intelligence Safety 2019 co-located with the 33rd AAAI Conference on Artificial Intelligence 2019 (AAAI)*, vol. 2301, 2019.
- [43] S. Thys, W. V. Ranst, and T. Goedemé, "Fooling automated surveillance cameras: Adversarial patches to attack person detection," in *IEEE Conference on Computer Vision and Pattern Recognition Workshops (CVPR Workshops)*, 2019, pp. 49–55.
- [44] V. Schwag, C. Sitawarin, A. N. Bhagoji, A. Mosenia, M. Chiang, and P. Mittal, "Not all pixels are born equal: An analysis of evasion attacks under locality constraints," in *Proceedings of the 2018 ACM SIGSAC Conference on Computer and Communications Security (CCS)*, 2018, pp. 2285–2287.
- [45] T. Gu, B. Dolan-Gavitt, and S. Garg, "BadNets: Identifying vulnerabilities in the machine learning model supply chain," in *Machine Learning and Computer Security Workshop (NeurIPS MLSec)*, 2017.
- [46] Y. Liu, S. Ma, Y. Aafer, W. Lee, J. Zhai, W. Wang, and X. Zhang, "Trojaning attack on neural networks," in *25th Annual Network and Distributed System Security Symposium (NDSS)*, 2018.
- [47] M. Sharif, S. Bhagavatula, L. Bauer, and M. K. Reiter, "Accessorize to a crime: Real and stealthy attacks on state-of-the-art face recognition," in *Proceedings of the 2016 ACM SIGSAC Conference on Computer and Communications Security (CCS)*, 2016, pp. 1528–1540.
- [48] H. Le and A. Borji, "What are the receptive, effective receptive, and projective fields of neurons in convolutional neural networks?" *arXiv preprint arXiv:1705.07049*, 2017.
- [49] W. Luo, Y. Li, R. Urtasun, and R. S. Zemel, "Understanding the effective receptive field in deep convolutional neural networks," in *Advances in Neural Information Processing Systems (NeurIPS)*, 2016, pp. 4898–4906.
- [50] A. Raghunathan, J. Steinhardt, and P. Liang, "Certified defenses against adversarial examples," in *6th International Conference on Learning Representations (ICLR)*, 2018.
- [51] E. Wong and J. Z. Kolter, "Provable defenses against adversarial examples via the convex outer adversarial polytope," in *Proceedings of the 35th International Conference on Machine Learning (ICML)*, 2018, pp. 5283–5292.
- [52] M. Lécuyer, V. Atlidakis, R. Geambasu, D. Hsu, and S. Jana, "Certified robustness to adversarial examples with differential privacy," in *2019 IEEE Symposium on Security and Privacy (S&P)*, 2019, pp. 656–672.
- [53] J. M. Cohen, E. Rosenfeld, and J. Z. Kolter, "Certified adversarial robustness via randomized smoothing," in *Proceedings of the 36th International Conference on Machine Learning (ICML)*, 2019, pp. 1310–1320.
- [54] H. Salman, J. Li, I. P. Razenshteyn, P. Zhang, H. Zhang, S. Bubeck, and G. Yang, "Provably robust deep learning via adversarially trained smoothed classifiers," in *Annual Conference on Neural Information Processing Systems 2019 (NeurIPS)*, 2019, pp. 11 289–11 300.
- [55] A. N. Bhagoji, D. Cullina, and P. Mittal, "Lower bounds on adversarial robustness from optimal transport," in *Advances in Neural Information Processing Systems (NeurIPS)*, 2019, pp. 7496–7508.
- [56] D. Cullina, A. N. Bhagoji, and P. Mittal, "Pac-learning in the presence of adversaries," in *Advances in Neural Information Processing Systems (NeurIPS)*, 2018, pp. 230–241.
- [57] E. Dohmatob, "Generalized no free lunch theorem for adversarial robustness," in *Proceedings of the 36th International Conference on Machine Learning (ICML)*, 2019, pp. 1646–1654.
- [58] D. Yin, R. Kannan, and P. Bartlett, "Rademacher complexity for adversarially robust generalization," in *Proceedings of the 36th International Conference on Machine Learning (ICML)*, 2019, pp. 7085–7094.
- [59] L. Schmidt, S. Santurkar, D. Tsipras, K. Talwar, and A. Madry, "Adversarially robust generalization requires more data," in *Advances in Neural Information Processing Systems*, 2018, pp. 5014–5026.
- [60] N. Papernot, P. McDaniel, A. Sinha, and M. P. Wellman, "Sok: Security and privacy in machine learning," in *2018 IEEE European Symposium on Security and Privacy (EuroS&P)*, 2018, pp. 399–414.
- [61] X. Yuan, P. He, Q. Zhu, and X. Li, "Adversarial examples: Attacks and defenses for deep learning," *IEEE transactions on neural networks and learning systems*, vol. 30, no. 9, pp. 2805–2824, 2019.
- [62] I. Feinerer and K. Hornik, *wordnet: WordNet Interface*, 2017, r package version 0.1-14. [Online]. Available: <https://CRAN.R-project.org/package=wordnet>
- [63] A. Paszke, S. Gross, F. Massa, A. Lerer, J. Bradbury, G. Chanan, T. Killeen, Z. Lin, N. Gimelshein, L. Antiga, A. Desmaison, A. Köpf, E. Yang, Z. DeVito, M. Raison, A. Tejani, S. Chilamkurthy, B. Steiner, L. Fang, J. Bai, and S. Chintala, "Pytorch: An imperative style, high-performance deep learning library," in *Annual Conference on Neural Information Processing Systems (NeurIPS)*, 2019, pp. 8024–8035.

A. Details of Experiment Setup

In this subsection, we provide additional details for datasets and model training. Our code is available at <https://github.com/inspire-group/PatchGuard> for the purpose of reproducibility.

ImageNet. ImageNet [24] is a popular benchmark dataset for high-resolution image classification. It has 1281167 training images and 50000 validation images from 1000 classes organized according to the WordNet [62] hierarchy. It is conventional to resize and crop ImageNet images to 224×224 or 299×299 . For ResNet, we take 224×224 images as inputs and use the pre-trained model from [38]. For BagNet, we take 224×224 inputs and use pre-trained models from [37]. For DS-ResNet-50, we use 299×299 images and use pre-trained models from [36]. The actual input of the base classifier of DS-ResNet-50 is a pixel patch in the shape of 25×299 ; DS-ResNet-50 counts the predictions from all possible 25×299 pixel patches and predicts the class with the largest count. When the confidence of local prediction is lower than 0.2, the base model will abstain from prediction.

ImageNette. ImageNette [27] is a subset of ImageNet with 9469 training images and 3925 validation images from classes of tench, English springer, cassette player, chain saw, church, French horn, garbage truck, gas pump, golf ball, parachute. We use this smaller dataset for a more comprehensive defense evaluation. We use the same model architectures as the models for ImageNet, but modify the last fully-connected layer (i.e., the classification layer) to accommodate for 10-class classification. We use the pre-trained models [36]–[38], retrain the entire model for 20 epochs with a batch size of 64, and retain the model with the highest validation accuracy. We use Stochastic Gradient Descent (SGD) with a 0.001 initial learning rate and a 0.9 momentum for model training. We reduce the learning rate with a factor of 0.1 every 7 epochs.

CIFAR-10. CIFAR-10 [28] is a benchmark dataset for low-resolution image classification. CIFAR-10 has 50000 training images and 10000 test images from classes plane, car, bird, cat, deer, dog, frog, horse, ship, truck. Each image is in the shape of 32×32 . For ResNet, we train the model from scratch for 20 epochs. We use SGD with a 0.01 initial learning rate, a 0.9 momentum, and a $5e-4$ weight decay. We reduce the learning rate with a factor of 0.1 every 10 epochs. For BagNet, we re-scale the 32×32 images to 192×192 with bicubic interpolation because we find BagNet does not have good performance on low-resolution images. We use the models [37] pre-trained on ImageNet and retrain the entire model with the same hyperparameters as we retrain a BagNet. For DS-ResNet-18, we take a 4×32 pixel band as the input to its base classifier and use the pre-trained model from [36]. Note that DS-ResNet-18 is based on the structure of ResNet-18 while other models are based on ResNet-50. The reported clean accuracy of ResNet-50 in Table IV is obtained from ResNet-50 retrained on 192×192 images, facilitating

comparison with the clean accuracy of BagNet-17 trained on re-scaled images.

Hardware and software. All of our experiments are done on a workstation with 32 Intel Xeon E5-2620 v4 CPU cores, 252GB RAM, and 8 NVIDIA Tesla P100 GPU. Timing results are obtained using one GPU and one CPU core. The deep learning models are implemented with PyTorch [63].

B. Additional results on attacked local logits

In section III-A, we show that the adversarial patches tend to create abnormally large local feature values to dominate the global prediction. In Figure 5 and Figure 6, we provide additional results for ImageNette and CIFAR-10. We can see that these results are similar to our observation for ImageNet. These results motivate our *robust masking* defense for a secure feature aggregation.

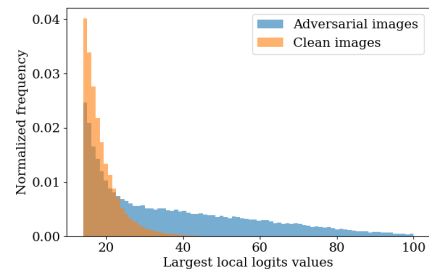


Fig. 5. Histogram of largest local logits values for adversarial and clean images for ImageNette.

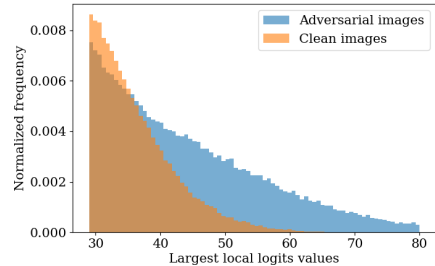


Fig. 6. Histogram of largest local logits values for adversarial and clean images for CIFAR-10.

C. Details of Receptive Fields

The focus on the center of the receptive field. In Section III-A and Section VI-B, we mentioned that a particular local feature focuses exponentially more on the center of its receptive field. We provide the intuition for this argument in Figure 7. The left part of the figure illustrates a 1-D example of convolution computation in which the input has five cells and will go through two convolution layers with a kernel size of 3 to compute the final output. Each cell in the hidden layer (i.e., the output of the first convolution layer) looks at 3 input cells, and the output cell looks at three hidden cells. We count the number of times each cell is looked at when computing the

output cell and plot it in the figure. As we can see, the center cell of the input layer receives the most attention (being looked at 3 times). Moreover, as the number of layers increases (a similar example for 3 convolution layers is plotted in the right part of Figure 7), the difference in attention between the center cell and the rightmost/leftmost cell will increase exponentially. Therefore, a particular feature focuses exponentially more on the center of its receptive field, and an adversary controlling the center cell will have a larger capacity to manipulate the final output features.

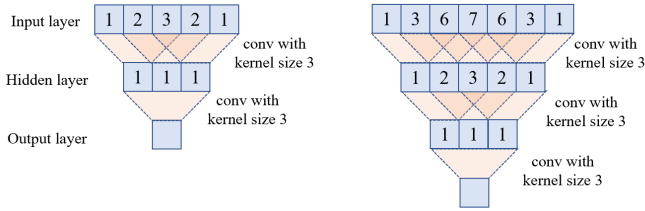


Fig. 7. Toy example of 1-D convolution computation

Computing the Window Size. One crucial step of our robust masking defense is to determine the window size, and we show in Section III-D and Equation 2 that the window size w can be computed as $w = \lceil (p + r - 1) / s \rceil$, where p is the patch size, r is the size of receptive field, and s is the stride of receptive field. In Figure 8, we provide the intuition for Equation 2. In this example, we assume the stride $s = 4$, and the size of the receptive field $r = 3$. We distinguish the centers of receptive fields, the other cells in the receptive fields, and the other cells with different colors. Note that we choose a large stride s such that adjacent receptive fields do not overlap for a better visual demonstration; the derived equation is applicable to smaller s or larger r . In Figure 8, we want to determine the largest patch size p such that the patch only appears in n but not $n+1$ receptive fields. We plot the boundary of the largest patch with red dash line in the figure. The left part of the patch covers the rightmost cells of receptive field 0, and the right part does not appear in receptive field n . Based on Figure 8, we can compute $p = n \cdot s - r + 1$. Next, we can substitute n with w , use $\lceil \cdot \rceil$ for generalization to any patch size, and finally get $w = \lceil (p + r - 1) / s \rceil$.

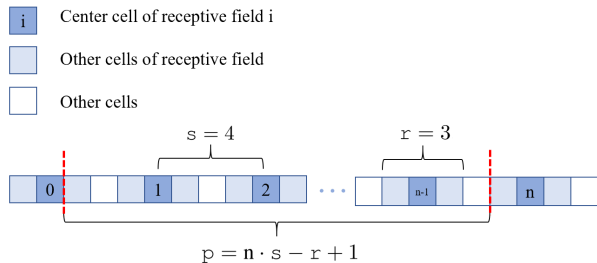


Fig. 8. Example of computing window size.

D. Additional results for CIFAR-10

In section V-C, we provide a detailed analysis of our defense on ImageNette. In this subsection, we provide additional results for CIFAR-10. We will report defense performance against a 2×2 (0.4% pixels), 5×5 (2.4%), and 8×8 (6.2%) adversarial patch. We re-scale the 32×32 images to 192×192 with bicubic interpolation and use BagNet-17 for most of the evaluation. Note that the patch size is also re-scaled proportionally.

Prediction invariance of vanilla models to feature masking. For BagNet-17 on a re-scaled 192×192 image, we will have 22×22 local features. The results for prediction invariance to feature masking are reported in Table XIV. We can see that the model predictions are generally invariant to small masks. However, we do find that BagNet is more sensitive to feature masking on CIFAR-10 than on ImageNet (Table VII), which also explains its relatively weaker provable robustness performance on CIFAR-10.

TABLE XIV
INVARIANCE OF BAGNET-17 PREDICTIONS TO FEATURE MASKING
(CIFAR-10)

| Window size | 0×0 | 2×2 | 4×4 | 6×6 | 8×8 |
|---------------------|--------------|--------------|--------------|--------------|--------------|
| Masked accuracy | 86.7% | 86.6% | 86.4% | 85.9% | 84.8% |
| % images | 13.3% | 18.7% | 23.4% | 29.0% | 34.7% |
| % windows per image | 0% | 0.4% | 1.1% | 2.3% | 4.0% |

Effect of clipping on vanilla models. We report the effect of clipping in Table XV. We also find models trained on CIFAR-10 are more sensitive to clipping than those trained on ImageNet (Table VIII). Our explanation is that most of the small pixel patches of tiny images like CIFAR-10 contain too little visual information and are even unrecognizable for a human. Therefore, most local predictions are incorrect, and the correct local prediction has to use large logits values to dominate the global prediction, which leads to the sensitivity to clipping.

TABLE XV
EFFECT OF LOGITS CLIPPING VALUES ON VANILLA MODELS (CIFAR-10)

| (c_l, c_h) | $(-\infty, \infty)$ | $(0, \infty)$ | $(0, 50)$ | $(0, 15)$ | $(0, 5)$ |
|--------------|---------------------|---------------|-----------|-----------|----------|
| ResNet-50 | 97.0% | 97.0% | 97.0% | 96.7% | 93.9% |
| BagNet-33 | 92.1% | 91.2% | 90.2% | 86.8% | 79.6% |
| BagNet-17 | 86.7% | 84.1% | 83.6% | 73.3% | 57.8% |
| BagNet-9 | 80.4% | 74.3% | 74.2% | 61.0% | 46.5% |

Effect of receptive field sizes on defended models. We report clean accuracy and provable robust accuracy of our defense for BagNet-33, BagNet-17, and BagNet-9, which have a receptive field of 33×33 , 17×17 , and 9×9 , respectively, against different patch sizes in Table XVI. The observation is similar to results for ImageNette in Table IX: a model with a larger receptive field has better clean accuracy but a larger receptive field results in a larger fraction of corrupted features and thus a larger gap between clean accuracy and provable robust accuracy.

TABLE XVI
EFFECT OF RECEPTIVE FIELD SIZES ON PROVABLE ROBUST ACCURACY (CIFAR-10)

| Patch size | 0.4% pixels | | 2.4% pixels | | 6.2% pixels | |
|------------|-------------|-------|-------------|-------|-------------|-------|
| | clean | adv. | clean | adv. | clean | adv. |
| BagNet-33 | 84.0% | 51.4% | 80.4% | 26.2% | 76.0% | 6.0% |
| BagNet-17 | 79.5% | 58.6% | 76.2% | 37.2% | 72.2% | 15.5% |
| BagNet-9 | 72.0% | 55.0% | 69.5% | 37.6% | 66.3% | 17.8% |

Effect of the detection threshold on defended models. We study the model performance of BagNet-17 against a 2.4% pixel patch as we change the detection threshold T from 0.0 to 1.0. The results are reported in Table XVII and are similar to those for ImageNette in Table X.

Breakdown of provable analysis on defended models. The breakdown of four failure cases of our provable analysis is reported in the right part of Table XVII. These observations are also similar to ImageNette in Table X.

TABLE XVII
PROVABLE ACCURACY AND FAILURE CASE BREAKDOWN OF BAGNET-17 WITH DIFFERENT DETECTION THRESHOLDS (CIFAR-10)

| | Clean | Provable | FP | Case I / IV | Case II | Case III |
|-------|-------|----------|-------|-------------|---------|----------|
| T-0.0 | 76.2% | 37.2% | 76.2% | 1.1% | 24.3% | 21.4% |
| T-0.2 | 77.8% | 31.7% | 51.1% | 41.4% | 4.7% | 6.3% |
| T-0.4 | 83.6% | 6.2% | 1.2% | 77.6% | 0.05% | 0.3% |
| T-0.6 | 84.1% | 0.2% | 0.02% | 83.9% | 0% | 0% |
| T-0.8 | 84.1% | 0% | 0% | 84.1% | 0% | 0% |
| T-1.0 | 84.1% | 0% | 0% | 84.1% | 0% | 0% |

Effect of using different feature types for defended models. The results for BagNet-17 with different features are reported in Table XVIII. Using logits as the feature type has a much better performance than confidence and prediction in terms of clean accuracy and provable accuracy. Results for Mask-DS are shown in Table XIX. Mask-DS works better when we use prediction or confidence as feature types due to its different training objectives.

TABLE XVIII
EFFECT OF FEATURE TYPES ON MASK-BN (CIFAR-10)

| Patch size | 0.4% pixels | | 2.4% pixels | | 6.2% pixels | |
|------------|-------------|-------|-------------|-------|-------------|-------|
| | clean | adv. | clean | adv. | clean | adv. |
| Logits | 79.5% | 58.6% | 76.2% | 37.2% | 72.2% | 15.5% |
| Confidence | 58.3% | 44.7% | 57.2% | 33.7% | 55.0% | 21.5% |
| Prediction | 53.0% | 38.4% | 52.7% | 27.4% | 51.9% | 16.7% |

Model inference efficiency. We report the per-image inference time in Table XX. We include results for the original 32×32 and re-scaled 192×192 images. The observation is similar to ImageNette in Table XIII. DS-ResNet requires a much longer inference time; robust masking incurs little defense overhead.

TABLE XIX
EFFECT OF FEATURE TYPES ON MASK-DS (CIFAR-10)

| Patch size | 0.4% pixels | | 2.4% pixels | | 6.2% pixels | |
|------------|-------------|-------|-------------|-------|-------------|-------|
| | clean | adv. | clean | adv. | clean | adv. |
| Logits | 82.9% | 64.3% | 80.5% | 43.1% | 77.7% | 17.7% |
| Confidence | 82.6% | 72.1% | 80.0% | 62.2% | 77.1% | 48.2% |
| Prediction | 82.5% | 71.9% | 80.4% | 61.3% | 77.6% | 47.8% |

TABLE XX
PER-IMAGE INFERENCE TIME OF DIFFERENT MODELS ON CIFAR-10

| Model | ResNet-50 | ResNet-50 | BagNet-17 | Mask-BN | ResNet-18 | DS-4-ResNet-18 | Mask-DS |
|------------|----------------|------------------|------------------|------------------|----------------|----------------|----------------|
| Image size | 32×32 | 192×192 | 192×192 | 192×192 | 32×32 | 32×32 | 32×32 |
| Time | 11.9ms | 12.7ms | 13.1ms | 13.7ms | 5.9ms | 122.2ms | 122.4ms |

E. Detailed Comparison Between Robust Masking and De-randomized Smoothing

In Section VI-A, we discussed that PatchGuard is a generalization of DS-ResNet [22], and our robust masking outperforms DS-ResNet due to the utilization of spatial information and tighter certification threshold. In this subsection, we provide more details supporting these two claims.

Spatial information. We will demonstrate the effect of spatial information in the certification process with a toy example. Assume the original local prediction vector for an image is $[C, C, W, C, C, W, C, C, W, C, C]$, where C refers to a correct prediction and W refers to a wrong prediction, and the adversary can additionally corrupt 3 local predictions. In this example, there are 8 correct predictions and 3 wrong predictions in the original prediction vector. Since their difference (5) is smaller than two times the upper bound of the number of corrupted predictions ($2 \cdot 3 = 6$), DS cannot certify this image. However, the adversary can only corrupt 3 *consecutive* local predictions, and the optimal attack can result in 6 correct predictions and 5 wrong predictions, which means this image should be certified. On the other hand, our robust masking utilizes the spatial information and can certify this image, leading to a better provable robustness.

Certification threshold. Let k be the upper bound on the number of corrupted features, and let the minimum change the adversary needs for achieving a successful attack be δ . In DS, the certification condition is $\delta > 2k$. In robust masking with feature type of prediction, we have $\text{SUM}(\mathbf{w}) = k$. From Algorithm 2, we have $s_2 = \text{SUM}(\mathbf{w}^* \odot \hat{\mathbf{u}}_y) < \text{SUM}(\mathbf{w}^*) = k$, and $s_3 = \text{SUM}(\mathbf{w}^* \odot \hat{\mathbf{u}}_y \odot (\mathbf{1} - \mathbf{w})) < \text{SUM}(\mathbf{w}^*) = k$. Our condition for certification becomes $\delta > s_2 > k$ or $\delta > s_3 > k$, which is easier to satisfy than $\delta > 2k$.

F. Empirical Results for Alternative Secure Aggregation Mechanisms

In Section VI-B, we discuss the use of alternative secure aggregation mechanisms. In this subsection, we provide an additional empirical analysis. In Table XXI, we report the empirical clean accuracy and robust accuracy against an adaptive attacker (one 2% pixel patch at a random location for each image) for mean aggregation (Mean), clipping with

$\tanh(0.05 \cdot \mathbf{u} - 1)$ (CBN), clipping with $c_l = 0, c_h = 15$ (Clip-15) and median aggregation (Median) on ImageNette. We can see CBN, Clip-15, and Median achieve a much better empirical adversarial accuracy than Mean. Table XXI also shows that ResNet can benefit from secure aggregation despite its large receptive fields, though its robustness is not as good as BagNet. We believe this is due to the limited influence of an adversarial patch far away from the receptive field center of the local feature (Appendix C), and this observation further motivates our future work on the “soft” constraint on the size of the receptive field.

TABLE XXI
CLEAN AND EMPIRICAL ADVERSARIAL ACCURACY AGAINST AN
ADAPTIVE ATTACKER FOR DIFFERENT AGGREGATIONS ON IMAGENETTE

| Aggregation Accuracy | Mean | | CBN [21] | | Clip-15 | | Median | |
|-------------------------|-------|-------|----------|-------|---------|-------|--------|-------|
| | clean | adv. | clean | adv. | clean | adv. | clean | adv. |
| ResNet-50 | 99.6% | 14.9% | 99.5% | 49.0% | 99.6% | 53.8% | 98.7% | 76.8% |
| BagNet-17 | 95.8% | 11.7% | 94.9% | 87.5% | 92.1% | 85.8% | 82.6% | 81.8% |